

Carbon and oxygen abundances from recombination lines in low-metallicity star-forming galaxies. Implications for chemical evolution^{*}

C. Esteban^{1,2,†}, J. García-Rojas^{1,2}, L. Carigi³, M. Peimbert³, F. Bresolin⁴,
A. R. López-Sánchez^{5,6}, A. Mesa-Delgado⁷

¹*Instituto de Astrofísica de Canarias, E-38200 La Laguna, Tenerife, Spain*

²*Departamento de Astrofísica, Universidad de La Laguna, E-38206, La Laguna, Tenerife, Spain*

³*Instituto de Astronomía, UNAM, Apdo. Postal 70-264, 04510 México D.F., Mexico*

⁴*Institute for Astronomy, 2680 Woodlawn Drive, Honolulu, HI 96822, USA*

⁵*Australian Astronomical Observatory, PO Box 915, North Ryde, NSW 1670, Australia*

⁶*Department of Physics and Astronomy, Macquarie University, NSW 2109, Australia*

⁷*Departamento de Astronomía y Astrofísica, Facultad de Física, Pontificia Universidad Católica de Chile, Av. Vicuña Mackenna 4860, 782-0436 Macul, Santiago, Chile*

Accepted 2014 June 12. Received 2014 June 12; in original form 2014 May 5

ABSTRACT

We present deep echelle spectrophotometry of the brightest emission-line knots of the star-forming galaxies He 2–10, Mkn 1271, NGC 3125, NGC 5408, POX 4, SDSS J1253–0312, Tol 1457–262, Tol 1924–416 and the H II region Hubble V in the Local Group dwarf irregular galaxy NGC 6822. The data have been taken with the Very Large Telescope Ultraviolet-Visual Echelle Spectrograph in the 3100–10420 Å range. We determine electron densities and temperatures of the ionized gas from several emission-line intensity ratios for all the objects. We derive the ionic abundances of C²⁺ and/or O²⁺ from faint pure recombination lines (RLs) in several of the objects, permitting to derive their C/H and C/O ratios. We have explored the chemical evolution at low metallicities analysing the C/O *vs.* O/H, C/O *vs.* N/O and C/N *vs.* O/H relations for Galactic and extragalactic H II regions and comparing with results for halo stars and DLAs. We find that H II regions in star-forming dwarf galaxies occupy a different locus in the C/O *vs.* O/H diagram than those belonging to the inner discs of spiral galaxies, indicating their different chemical evolution histories, and that the bulk of C in the most metal-poor extragalactic H II regions should have the same origin than in halo stars. The comparison between the C/O ratios in H II regions and in stars of the Galactic thick and thin discs seems to give arguments to support the merging scenario for the origin of the Galactic thick disc. Finally, we find an apparent coupling between C and N enrichment at the usual metallicities determined for H II regions and that this coupling breaks in very low-metallicity objects.

Key words: H II regions – galaxies: abundances – galaxies: dwarf – galaxies: irregular – galaxies: ISM – galaxies: individual: He 2–10 – galaxies: individual: Mkn 1271 – galaxies: individual: NGC 3125 – galaxies: individual: NGC 5408 – galaxies: individual: NGC 6822 – galaxies: individual: POX 4 – galaxies: individual: SDSS J1253–0312 – galaxies: individual: Tol 1457–262 – galaxies: individual: Tol 1924–416

1 INTRODUCTION

Carbon is the most abundant heavy-element in the Universe after oxygen and has an indisputable biogenic significance. It is an important source of opacity and energy production in stars as well as a major constituent of interstellar dust and organic molecules. Despite its importance, we have very

^{*} Based on observations collected at the European Southern Observatory, Chile, proposal number ESO 081.C-0113(A).

[†] E-mail: cel@iac.es

few determinations of its abundance in external galaxies and they are based on the analysis of emission-line spectra of H II regions. The most prominent spectral features of C require observations from space. The brightest collisionally excited lines (hereafter CELs) of C in ionized nebulae are C III] 1909 Å and [C II] 2326 Å lines in the UV and the determination of its line fluxes is severely affected by uncertainties in the reddening correction. On the other hand, the far-IR [C II] 158 μm fine-structure line has the disadvantage that its emission arises predominantly in photodissociation regions, not in the ionized gas-phase. However, there are faint recombination lines (hereafter RLs) of C²⁺ in the optical that can be detected and measured in bright nebulae with the use of high-throughput spectrographs at large-aperture telescopes. The brightest of these RLs is C II 4267 Å, which has also the advantage of lying in a spectral zone free of blending with other emission lines. Some of us have been pioneer measuring the C II 4267 Å line in Galactic and extragalactic H II regions using intermediate and high-spectral resolution spectroscopy (e.g. Peimbert et al. 1992; Esteban et al. 2002, 2009; García-Rojas & Esteban 2007; López-Sánchez et al. 2007). In particular, we have obtained – for the first time – the C/H and C/O radial gradients of the ionized gas in the Milky Way (Esteban et al. 2005, 2013) and preliminary estimates for those gradients for the spiral galaxies M31, M33, M101 and NGC 2403 (see Esteban et al. 2014).

The C content in low-metallicity star-forming dwarf galaxies was first investigated by Garnett et al. (1995, 1997); Kobulnicky et al. (1997) and Kobulnicky & Skillman (1998) based on *Hubble Space Telescope* (*HST*) spectroscopy in the UV range that included measurements of the C III] 1909 Å line and also [C II] 2326 Å in some cases. These studies obtained data for a dozen metal-poor dwarf galaxies including I Zw 18, NGC 5253, NGC 4861, and NGC 2366. These works confirmed a rather clear correlation between the C/O and O/H ratios with C showing an apparent “secondary” behaviour with respect to O (Garnett 2004). The observed C/O *vs.* O/H trend has been interpreted as the time delay in the release of C by low- and intermediate-mass (LIM) stars with respect to the O production and/or metallicity-dependent yields of C in massive stars (Garnett et al. 1999; Henry et al. 2000; Carigi 2000; Chiappini et al. 2003).

The aim of the present paper is to detect and measure C II and O II RLs in low-metallicity H II regions of star-forming dwarf galaxies to explore the C content and the behaviour of the C/O ratio at low metallicities in combination with our previous data for H II regions in discs of the Milky Way and other nearby spiral galaxies. These determinations of the C/O ratios would be more solid than those based on UV CELs because they are much less dependent on uncertainties in the reddening law and the temperature structure of the nebulae.

The structure of this paper is as follows. In §2 we describe the sample selection, observations and the data reduction procedure. In §3 we describe the emission line measurements and identifications as well as the reddening correction. In §4 we present the physical conditions and ionic and total abundances determined for the sample objects. In §5 we discuss the behaviour of the C/O *vs.* O/H and C/O *vs.* N/O relations in low-metallicity objects. Finally, in §6 we summarize our main conclusions.

2 SAMPLE SELECTION, OBSERVATIONS AND DATA REDUCTION

The sample was selected after an inspection of the available literature collecting spectrophotometric data of H II galaxies and H II regions in dwarf irregular galaxies. In order to detect and measure the faint RLs of C II 4267 Å and those of multiplet 1 of O II at about 4650 Å, we selected objects that could be observed from Paranal Observatory showing: a) high surface brightness in the Hβ or Hα lines and b) high ionization degree to ensure a better chance to detect lines of C²⁺ and O²⁺. We also include the bright H II region Hubble V (HV) in the dwarf irregular galaxy of the Local Group NGC 6822. This is the only object for which C II and O II RLs were previously detected but from low spectral resolution data (Peimbert et al. 2005). Table 1 compiles the coordinates of the slit centre of our observations as well as the morphological classification, absolute magnitudes, and distances to the galaxies as it is usually indicated in the NED database. In the case of NGC 6822, these data have been taken from the compilation of McConnachie (2012) for galaxies of the Local Group. For POX 4 and Tol 1457–262 the values of *M_V* have been taken from López-Sánchez & Esteban (2008). In our sample objects, C II and O II lines were well measured –with an uncertainty better than 40% in their line intensity ratio with respect to Hβ– in NGC 5408, and NGC 6822. For Mrk 1271 and NGC 3125 we obtain good measurements of O II lines but only detections of C II. For POX 4, we measured C II and only a noisy detection of the O II lines. In SDSS J1253–312 we detected both kinds of RLs and only O II in Tol 1924–416. Unfortunately, for He 2–10 and Tol 1457–262 we did not detect the RLs of our interest. It is important to note that Guseva et al. (2011) used the data we are analysing in this paper as part of their study of archive data for determining abundance patterns and the abundance discrepancy in low-metallicity emission-line galaxies. These authors report good measurements of both, C II and O II lines in NGC 5408, NGC 6822 – like us – but also in Mrk 1271, NGC 3125, and POX 4. On the other hand, Guseva et al. (2011) give errors of about 35% for the C II 4267 Å line in Tol 1457–262, and Tol 1924–416, objects for which we do not detect this line at all. Perhaps, these differences can be explained attending to different extraction windows used in both studies. As it is indicated ahead in this section, our extraction windows were restricted to isolate the brightest knots but, unfortunately, Guseva et al. (2011) do not provide precise information about this issue.

The observations were made on 2008 May 2 and 3 at Cerro Paranal Observatory (Chile), using the UT2 (Kueyen) of the Very Large Telescope (VLT) with the Ultraviolet Visual Echelle Spectrograph (UVES, D’Odorico et al. 2000). The standard settings of UVES were used covering the spectral range from 3100 to 10420 Å. Some small spectral intervals could not be observed. These are: 5773–5833, 8535–8649, 10081–10091 and 10249–10262 Å due to the physical separation between the CCDs of the detector system of the red arm and because the last orders of the spectrum do not fit completely within the size of the CCD. The journal of the observations is shown in Table 1. The spectra are divided in four spectral ranges (B1, B2, R1, and R2 in Table 1) because of the two central wavelengths used to cover the whole optical-NIR with the two arms of UVES.

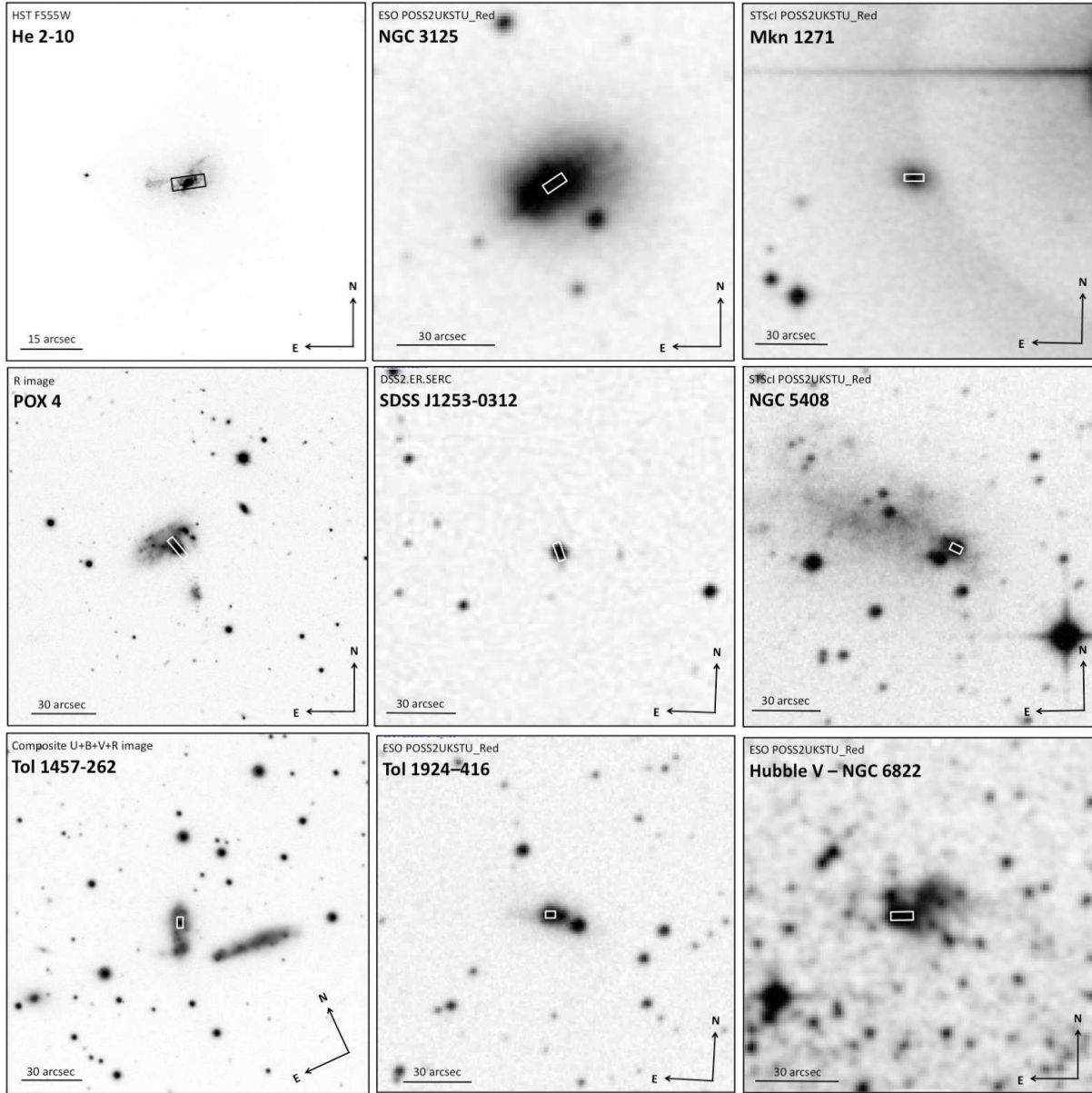


Figure 1. Finding charts of the objects based on optical images. open rectangles indicate the position and size of the areas extracted for spectroscopical analysis. All the images have been obtained from the Aladin interactive sky atlas (Bonnarel et al. 2000) except those of POX 4 and Tol 1457–262, which have been taken from López-Sánchez & Esteban (2008).

These spectral ranges are: 3100–3870 Å (B1), 3760–4985 Å (B2), 4785–6815 Å (R1) and 6700–10420 Å (R2). For some of the objects, additional single short exposures of 60 seconds were taken to obtain non-saturated flux measurements for the brightest emission lines. The slit was set at different position angles in the objects trying to cover the brightest areas. The atmospheric dispersion corrector (ADC) was used to keep the same observed region within the slit regardless of the airmass value. The slit width was set to 3'' ($R \sim 15,000\text{--}20,000$) as a compromise between the spectral resolution needed and the desired signal-to-noise ratio of the spectra. The slit length was fixed to 10'' in the two bluest spectral ranges (B1 and B2) and 12'' and the two reddest ones (R1 and R2). The final one-dimensional spectra we

analysed were extracted for areas of different size, covering the brightest knots of the objects but the same sizes in the blue and red spectral ranges. In Table 1 and Figure 1 we indicate the position and size of the areas extracted for each object.

The spectra were reduced using the IRAF¹ echelle reduction package, following the standard procedure of bias subtraction, aperture extraction, flatfielding, wavelength calibration and flux calibration. The standard stars LTT 3864,

¹ IRAF is distributed by NOAO, which is operated by AURA, under cooperative agreement with NSF.

Table 1. Basic data of the sample galaxies and journal of observations.

Object	R.A. ^a	Dec. ^a	Type ^b	M^c	d^d [Mpc]	P.A. [°]	Extracted Area [arcsec ²]	Exposure Time ^e (s)	
								B1 and R1	B2 and R2
He 2–10	08 36 15.0	−26 24 33	I0? pec	−19.0(R)	10.5	98	8×3	60, 3×400	60, 3×1600
NGC 3125	10 06 33.6	−29 56 08	BCDG	−19.2(R)	12.3	124	7×3	3×400	60, 3×1600
Mkn 1271	10 56 09.1	+06 10 22	Compact	−16.3(F_{pg})	13.7	90	8×3	60, 3×400	60, 3×1600
POX 4	11 51 11.7	−20 35 58	H II	−19.1(V)	47	40	8×3	3×400	3×1600
SDSS J1253–0312	12 53 06.0	−03 12 59	H II	−19.8(g)	92	20	8×3	3×400	3×1600
NGC 5408	14 03 15.5	−41 22 24	IB(s)m	−17.2(V)	4.9	62.4	5×3	60, 3×400	60, 3×1800
Tol 1457–262	15 00 27.1	−26 26 57	H II	−19.9(V)	68	155	5.5×3	3×400	3×1600
Tol 1924–416	19 27 58.0	−41 34 27	pec H II	−19.9(V)	39	91.7	4.25×3	3×400	3×1600
NGC 6822 (HV)	19 44 52.4	−14 43 13	IB(s)m	−15.2(V)	0.46	91	8×3	3×400	60, 3×1600

^a Coordinates of the slit centre (J2000.0).

^b Morphological type from NED database.

^c Absolute magnitude from NED database except for POX 4 and Tol 1457–262 (López-Sánchez & Esteban 2008) and NGC 6822 (McConnachie 2012). The band of the photometric data is in parenthesis.

^d Distance taken from NED database except for NGC 6822 (McConnachie 2012).

^e Spectral ranges observed B1: 3100–3870 Å; B2: 3760–4985 Å; R1: 4785–6815 Å; R2: 6700–10420 Å.

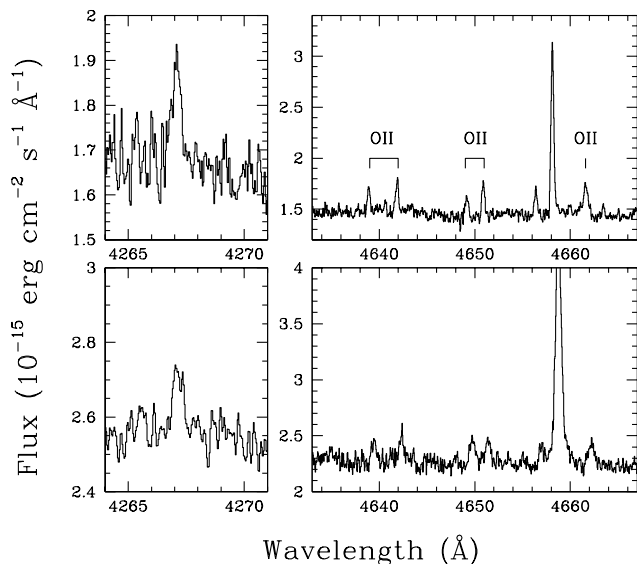


Figure 2. Sections of the UVES spectra – uncorrected for reddening – of HV (NGC 6822, upper panels) and NGC 5408 (lower panels) showing the recombination lines of C II 4267 Å (left) and multiplet 1 of O II about 4650 Å (right). The wavelengths have been corrected to their rest values.

CD−32°9927, and EG 274 (Hamuy et al. 1992, 1994) were observed to perform the flux calibration.

3 LINE INTENSITIES

Line fluxes were measured with the SPLIT routine of IRAF by integrating all the flux in the line between two given limits and over the average local continuum. In the case of line blending, a double Gaussian profile fit procedure was applied to measure the individual line intensities.

All line fluxes of a given spectrum have been normalized to a particular bright emission line in each spectral

range. For the bluest range (B1), the reference line was H10 3798 Å. For the B2 and R1 ranges, H β was used. For the reddest spectral interval, R2, the reference line was [S II]6717 Å. In order to produce a final homogeneous set of line flux ratios, all of them were rescaled to H β considering the $F(\text{H10})/F(\text{H}\beta)$ and $F([\text{S II}] 6717 \text{ \AA})/F(\text{H}\beta)$ line intensity ratios measured in the B2 and R1 spectral ranges, respectively.

The spectral ranges observed present some overlapping at the edges. The final flux of a line in the overlapping regions was the average of the values obtained in both adjacent spectra. A similar procedure was considered in the case of lines present in two consecutive spectral orders. The average of both measurements were considered as the adopted value of the line flux. In all cases, the differences in the line flux measured for the same line in different orders and/or spectral ranges do not show systematic trends and are always within the uncertainties.

The identification and laboratory wavelengths of the lines were obtained following our previous works on echelle spectroscopy of bright extragalactic H II regions (López-Sánchez et al. 2007; Esteban et al. 2009). For a given line, the observed wavelength is determined by the central point of the two extremes of the baseline chosen for the line flux integration or the centroid of the line when a Gaussian fit is used (in the case of line blending). The final adopted values of the observed wavelength of a given line are relative to the heliocentric reference frame.

The observed line intensities must be corrected for interstellar reddening. This was done using the reddening constant, $c(\text{H}\beta)$, obtained from the intensities of the Balmer lines. However, the fluxes of H I lines may be also affected by underlying stellar absorption. Consequently, we have performed an iterative procedure to derive both $c(\text{H}\beta)$ and the equivalent widths of the absorption in the H I lines, W_{abs} , which we use to correct the observed line intensities. We assumed that the equivalent width of the absorption components is the same for all the Balmer lines and used the relation given by Mazzarella & Boroson (1993) to the absorption correction for each Balmer line following the procedure

Table 2. Dereddened line intensity ratios with respect to $I(\text{H}\beta) = 100$ of HV (NGC 6822), NGC 5408, and Tol 1924–416.

λ_0 (Å)	Ion	ID	$f(\lambda)$	HV (NGC 6822)		NGC 5408		Tol 1924–416	
				λ (Å)	$I(\lambda)$	λ (Å)	$I(\lambda)$	λ (Å)	$I(\lambda)$
3187.84	He I	3	0.308	3187.16	0.72 ± 0.07	3193.11	1.13 ± 0.09	3217.88	1.7 ± 0.2
3342.85	[Cl III]	1F	0.304	–	–	3348.17	0.29 ± 0.05	–	–
3447.59	He I	7	0.295	3446.92	0.30 ± 0.04	3453.30	0.18 ± 0.04	3480.17	0.4 ± 0.1
3450.39	He I		0.295	–	–	3457.80	0.06:	–	–
3530.50	He I	36	0.286	–	–	3536.38	0.15 ± 0.04	–	–
3554.42	He I	34	0.283	3553.76	0.21 ± 0.04	3560.45	0.22 ± 0.05	–	–
3587.28	He I	3	0.278	3586.64	0.26 ± 0.04	3593.33	0.24 ± 0.05	–	–
3613.64	He I	6	0.275	3612.98	0.41 ± 0.05	3619.72	0.33 ± 0.05	3647.83	0.14:
3634.25	He I	28	0.272	3633.62	0.39 ± 0.05	3640.34	0.40 ± 0.06	3668.57	0.3 ± 0.1
3661.22	H I	H31	0.267	–	–	3667.39	0.15 ± 0.04	–	–
3662.26	H I	H30	0.267	–	–	3668.37	0.18 ± 0.04	–	–
3663.40	H I	H29	0.267	–	–	3669.56	0.23 ± 0.05	–	–
3664.68	H I	H28	0.267	3664.01	0.27 ± 0.04	3670.84	0.26 ± 0.05	–	–
3666.10	H I	H27	0.267	3665.42	0.37 ± 0.05	3672.21	0.30 ± 0.05	–	–
3667.68	H I	H26	0.266	3666.99	0.33 ± 0.04	3673.84	0.40 ± 0.05	–	–
3669.47	H I	H25	0.266	3668.78	0.39 ± 0.05	3675.64	0.39 ± 0.05	–	–
3671.48	H I	H24	0.266	3670.79	0.41 ± 0.05	3677.66	0.43 ± 0.06	3706.08	0.3 ± 0.1
3673.76	H I	H23	0.265	3673.07	0.45 ± 0.05	3679.92	0.47 ± 0.06	3708.45	0.4 ± 0.1
3676.37	H I	H22	0.265	3675.68	0.52 ± 0.05	3682.52	0.57 ± 0.06	3710.98	0.5 ± 0.1
3679.36	H I	H21	0.265	3678.67	0.71 ± 0.06	3685.52	0.64 ± 0.06	3714.03	0.5 ± 0.1
3682.81	H I	H20	0.264	3682.12	0.75 ± 0.07	3689.00	0.81 ± 0.07	3717.59	0.7 ± 0.1
3686.83	H I	H19	0.263	3686.14	0.81 ± 0.07	3693.03	0.87 ± 0.07	3721.70	0.9 ± 0.1
3691.56	H I	H18	0.263	3690.86	0.92 ± 0.08	3697.77	1.10 ± 0.08	3726.42	1.1 ± 0.1
3697.15	H I	H17	0.262	3696.47	1.10 ± 0.09	3703.35	1.28 ± 0.09	3732.09	1.3 ± 0.2
3703.86	H I	H16	0.260	3703.17	1.3 ± 0.1	3710.08	1.37 ± 0.09	3739.11	1.9 ± 0.2
3705.04	He I	25	0.260	3704.34	0.63 ± 0.06	3711.23	0.59 ± 0.06	–	–
3711.97	H I	H15	0.259	3711.29	1.6 ± 0.1	3718.21	1.6 ± 0.1	3747.03	1.6 ± 0.2
3721.83	[S III]	2F	0.257	3721.14	3.1 ± 0.2	3728.12	3.1 ± 0.2	3757.01	2.9 ± 0.2
3721.94	H I	H14							
3726.03	[O II]	1F	0.257	3725.34	49 ± 3	3732.29	39 ± 2	3761.24	57 ± 3
3728.82	[O II]	1F	0.256	3728.09	65 ± 3	3735.05	49 ± 2	3764.02	76 ± 3
3732.86	He I	24	0.256	–	–	3739.14	0.09:	–	–
3734.37	H I	H13	0.255	3733.68	2.3 ± 0.1	3740.65	2.4 ± 0.1	3769.62	2.1 ± 0.1
3750.15	H I	H12	0.253	3749.46	2.8 ± 0.2	3756.46	3.1 ± 0.2	3785.53	2.9 ± 0.2
3770.63	H I	H11	0.249	3769.94	3.8 ± 0.2	3776.95	3.9 ± 0.2	3806.22	3.6 ± 0.2
3797.90	H I	H10	0.244	3797.21	4.9 ± 0.3	3804.27	5.1 ± 0.2	3833.75	4.8 ± 0.2
3805.74	He I	58	0.242	3805.09	0.06 ± 0.01	3812.24	0.88 ± 0.05	–	–
3819.61	He I	22	0.240	3818.94	0.94 ± 0.06	3826.03	0.51 ± 0.03	3855.70	0.76 ± 0.06
3831.66	S II		0.238	3831.14	0.07 ± 0.01	–	–	–	–
3835.39	H I	H9	0.237	3834.69	6.5 ± 0.3	3841.82	6.9 ± 0.3	3871.60	6.5 ± 0.3
3856.02	Si II	1F	0.233	–	–	3862.42	0.07 ± 0.01	–	–
3856.13	O II	12							
3862.59	Si II	1	0.232	3861.86	0.07 ± 0.01	3869.00	0.08 ± 0.01	3899.01	0.22 ± 0.04
3867.49	He I	20	0.231	3866.81	0.10 ± 0.01	–	–	–	–
3868.75	[Ne III]	1F	0.230	3868.07	35 ± 2	3875.23	49 ± 2	3905.28	46 ± 2
3871.82	He I	60	0.230	3871.07	0.06 ± 0.01	3878.23	0.055 ± 0.009	–	–
3889.05	H I	H8	0.226	3888.17	17.9 ± 0.9	3895.37	18.9 ± 0.8	3925.59	18.5 ± 0.8
3926.53	He I	58	0.219	3925.82	0.11 ± 0.01	–	–	–	–
3964.73	He I	5	0.211	3964.02	0.84 ± 0.05	3971.35	0.72 ± 0.04	4002.16	0.63 ± 0.06
3967.46	[Ne III]	1F	0.211	3966.76	10.7 ± 0.5	3974.10	15.4 ± 0.7	4004.91	13.7 ± 0.6
3970.07	H I	H7	0.210	3969.36	14.4 ± 0.7	3976.71	15.7 ± 0.7	4007.55	15.3 ± 0.7
4009.22	He I	55	0.202	4008.47	0.21 ± 0.02	4015.95	0.16 ± 0.01	–	–
4026.21	He I	18	0.198	4025.48	1.80 ± 0.09	4032.94	1.81 ± 0.08	4064.26	1.8 ± 0.1
4068.60	[S II]	1F	0.189	4067.85	0.68 ± 0.04	4075.42	0.86 ± 0.04	4107.08	1.14 ± 0.08
4069.62	O II	10	0.189	4068.98	0.09 ± 0.01	–	–	–	–
4076.35	[S II]	1F	0.187	4075.61	0.25 ± 0.02	4083.11	0.27 ± 0.02	4114.81	0.37 ± 0.04
4085.11	O II	10	0.185	–	–	4091.50	0.045 ± 0.009	–	–
4100.62	D I	D6	0.182	4099.84	0.048 ± 0.009	–	–	–	–
4101.74	H I	H6	0.182	4100.99	25 ± 1	4108.60	25 ± 1	4140.46	25 ± 1
4120.82	He I	16	0.177	4120.07	0.19 ± 0.02	4127.71	0.23 ± 0.02	4159.63	0.12 ± 0.03
4143.76	He I	53	0.172	4143.00	0.25 ± 0.02	4150.69	0.27 ± 0.02	–	–
4168.97	He I	52	0.167	4168.29	0.08 ± 0.01	4175.86	0.055 ± 0.009	–	–

Table 2. *continued*

λ_0 (Å)	Ion	ID	$f(\lambda)$	HV (NGC 6822)		NGC 5408		Tol 1924–416	
				λ (Å)	$I(\lambda)$	λ (Å)	$I(\lambda)$	λ (Å)	$I(\lambda)$
4209.15	[Fe III]		0.157	4208.45	0.027 ± 0.007	—	—	—	—
4227.91	[Ni III]		0.153	—	—	4234.77	0.09 ± 0.01	—	—
4243.97	[Fe II]	21F	0.149	—	—	4251.08	0.027 ± 0.007	4284.05	0.07 ± 0.02
4267.15	C II	6	0.144	4266.36	0.046 ± 0.008	4274.18	0.020 ± 0.006	—	—
4276.83	[Fe II]	21F	0.142	—	—	4283.85	0.039 ± 0.008	4317.37	0.12 ± 0.03
4287.40	[Fe II]	7F	0.139	4286.60	0.039 ± 0.008	4294.53	0.11 ± 0.01	4327.76	0.28 ± 0.04
4317.14	O II	2	0.132	4316.32	0.028 ± 0.007	—	—	—	—
4340.47	H I	H γ	0.127	4339.68	44 ± 2	4347.72	48 ± 2	4381.45	46 ± 2
4359.34	[Fe II]	7F	0.122	—	—	4366.60	0.07 ± 0.01	4400.48	0.13 ± 0.03
4363.21	[O III]	2F	0.121	4362.43	5.5 ± 0.2	4370.50	12.0 ± 0.5	4404.37	9.4 ± 0.4
4368.19	O I	5	0.120	—	—	4375.58	0.07 ± 0.01	4409.44	0.09 ± 0.03
4368.25	O I	5							
4387.93	He I	51	0.115	4387.14	0.48 ± 0.03	—	—	4429.33	0.41 ± 0.04
4413.78	[Fe II]	7F	0.109	—	—	4421.09	0.08 ± 0.01	4455.42	0.11 ± 0.03
4415.09	O I	5	0.109	—	—	4423.69	0.025 ± 0.007	—	—
4437.55	He I	50	0.104	4436.74	0.063 ± 0.009	4445.00	0.08 ± 0.01	—	—
4452.11	[Fe II]	7F	0.100	—	—	4459.54	0.029 ± 0.007	4494.00	0.08 ± 0.02
4457.95	[Fe II]	6F	0.099	—	—	—	—	4499.94	0.05:
4471.48	He I	14	0.096	4470.70	3.8 ± 0.2	4478.98	3.9 ± 0.1	4513.75	3.9 ± 0.2
4474.91	[Fe II]	7F	0.095	—	—	4484.79	0.039 ± 0.008	—	—
4514.9	[Fe II]	6F	0.085	—	—	—	—	4558.77	0.05:
4562.60	[Mg I]		0.073	4561.78	0.10 ± 0.01	4570.19	0.16 ± 0.01	4605.68	0.29 ± 0.04
4565.20	?		0.073	—	—	4572.73	0.035 ± 0.007	—	—
4571.10	Mg I]		0.071	4570.26	0.072 ± 0.009	4578.70	0.13 ± 0.01	4614.18	0.12 ± 0.03
4607.13	[Fe III]	3F	0.062	—	—	4614.88	0.021 ± 0.006	4650.31	0.08 ± 0.02
4609.44	O II	93	0.062	—	—	4617.99	0.034 ± 0.007	—	—
4610.20	O II		0.062	4609.42	0.030 ± 0.007	—	—	—	—
4638.86	O II	1	0.055	4638.03	0.030 ± 0.006	4646.59	0.034 ± 0.007	—	—
4640.64	N III	2	0.054	4639.78	0.009:	—	—	—	—
4641.81	O II	1	0.054	4640.99	0.041 ± 0.007	4649.46	0.038 ± 0.008	4685.80	0.03:
4643.06	N II	5	0.054	4642.53	0.009:	—	—	—	—
4649.13	O II	1	0.052	4648.30	0.037 ± 0.007	4656.90	0.039 ± 0.008	—	—
4650.84	O II	1	0.052	4650.02	0.044 ± 0.007	4658.53	0.033 ± 0.007	4694.64	0.03:
4656.4	Si ?		0.050	—	—	4664.15	0.025 ± 0.007	—	—
4658.10	[Fe III]	3F	0.050	4657.27	0.23 ± 0.02	4665.91	0.44 ± 0.02	4702.17	0.96 ± 0.06
4661.63	O II	1	0.049	4660.71	0.076 ± 0.009	4669.34	0.037 ± 0.008	—	—
4667.01	[Fe III]	3F	0.048	—	—	4674.86	0.023 ± 0.006	—	—
4676.24	O II	1	0.046	4675.42	0.032 ± 0.007	4683.99	0.015 ± 0.005	—	—
4685.71	He II		0.043	—	—	4693.86	0.82 ± 0.04	4730.05	0.74 ± 0.05
4701.53	[Fe III]	3F	0.039	4700.70	0.064 ± 0.009	4709.44	0.11 ± 0.01	4745.80	0.25 ± 0.04
4703.30	O I ?		0.039	—	—	4711.32	0.031 ± 0.007	—	—
4711.37	[Ar IV]	1F	0.037	4710.56	0.33 ± 0.02	4719.30	1.46 ± 0.06	4755.74	0.95 ± 0.06
4713.14	He I	12	0.036	4712.32	0.43 ± 0.02	4721.05	0.58 ± 0.03	4757.61	0.49 ± 0.05
4733.93	[Fe III]	3F	0.031	4733.02	0.018 ± 0.005	—	—	4778.82	0.12 ± 0.03
4740.16	[Ar IV]	1F	0.030	4739.40	0.24 ± 0.02	4748.20	1.20 ± 0.05	4784.85	0.74 ± 0.05
4751.2	Ca I ?		0.027	—	—	4759.35	0.051 ± 0.008	—	—
4754.83	[Fe III]	3F	0.026	4753.86	0.040 ± 0.007	4762.77	0.07 ± 0.01	4799.65	0.17 ± 0.03
4769.60	[Fe III]	3F	0.023	4768.55	0.015 ± 0.005	4777.50	0.038 ± 0.008	4814.63	0.09 ± 0.02
4777.88	[Fe III]	3F	0.021	—	—	4785.63	0.019 ± 0.006	—	—
4788.13	N II	20	0.018	—	—	4796.52	0.015 ± 0.005	—	—
4800.24	O I ?		0.015	—	—	4808.46	0.040 ± 0.008	—	—
4814.55	[Fe II]	20F	0.012	—	—	4822.51	0.028 ± 0.007	—	—
4850.1	Ca I ?		0.003	—	—	4858.50	0.053 ± 0.008	—	—
4861.33	H I	H β	0.000	4860.45	100 ± 4	4869.47	100 ± 4	4907.23	100 ± 4
4881	[Fe III]	2F	-0.005	4880.18	0.078 ± 0.009	4889.20	0.12 ± 0.01	4927.07	0.26 ± 0.03
4901.43	[Ni II]		-0.010	—	—	4909.67	0.08 ± 0.01	—	—
4902.65	Si II	7.23	-0.010	4901.82	0.034 ± 0.006	4911.07	0.043 ± 0.008	—	—
4905.34	[Fe II]	20F	-0.011	—	—	4914.92	0.16 ± 0.01	—	—
4921.93	He I	48	-0.015	4921.05	1.04 ± 0.05	4930.16	1.06 ± 0.04	4968.40	0.98 ± 0.06
4924.5	[Fe III]	2F	-0.016	4923.65	0.025 ± 0.006	—	—	—	—
4931.32	[O III]	1F	-0.017	4930.37	0.065 ± 0.008	4939.40	0.08 ± 0.01	—	—
4958.91	[O III]	1F	-0.024	4958.04	181 ± 7	4967.26	217 ± 8	5005.76	202 ± 7

Table 2. *continued*

λ_0 (Å)	Ion	ID	$f(\lambda)$	HV (NGC 6822)		NGC 5408		Tol 1924–416	
				λ (Å)	$I(\lambda)$	λ (Å)	$I(\lambda)$	λ (Å)	$I(\lambda)$
4985.9	[Fe III]	2F	-0.031	4984.91	0.17 ± 0.01	4994.25	0.31 ± 0.02	5033.00	1.12 ± 0.08
5006.84	[O III]	1F	-0.036	5005.96	541 ± 22	5015.30	544 ± 19	5054.14	608 ± 21
5015.68	He I	4	-0.038	5014.78	2.21 ± 0.09	5024.11	1.98 ± 0.08	5063.05	2.0 ± 0.1
5041.03	Si II	5	-0.044	5040.02	0.09:	5049.48	0.11 ± 0.02	—	—
5055.98	Si II	5	-0.048	—	—	5064.52	0.05 ± 0.01	—	—
5158.81	[Fe II]	19F	-0.091	—	—	—	—	5207.33	0.14 ± 0.04
5191.82	[Ar III]	3F	-0.081	5190.75	0.12 ± 0.03	—	—	—	—
5197.90	[N I]	1F	-0.082	5196.96	0.15 ± 0.03	5206.64	0.26 ± 0.02	5246.98	0.43 ± 0.05
5200.26	[N I]	1F	-0.083	5199.31	0.07:	5208.97	0.12 ± 0.02	5249.36	0.22 ± 0.04
5261.62	[Fe II]	19F	-0.109	—	—	5270.46	0.03 ± 0.01	—	—
5270.40	[Fe III]	1F	-0.111	5269.52	0.10 ± 0.03	5279.37	0.17 ± 0.02	—	—
5273.38	[Fe II]	18F	-0.111	—	—	5282.21	0.04 ± 0.01	—	—
5517.71	[Cl III]	1F	-0.154	5516.69	0.42 ± 0.03	5526.97	0.31 ± 0.02	5569.90	0.31 ± 0.05
5537.88	[Cl III]	1F	-0.158	5536.82	0.32 ± 0.03	5547.12	0.21 ± 0.02	5589.89	0.29 ± 0.05
5554.83	O I	24	-0.160	—	—	5564.00	0.04 ± 0.01	—	—
5555.03	O I	24	—	—	—	—	—	—	—
5577.34	[O I]	3F	-0.164	—	—	5586.70	0.022 ± 0.009	—	—
5754.64	[N II]	3F	-0.194	5753.52	0.11 ± 0.03	5764.22	0.07 ± 0.01	—	—
5875.64	He I	11	-0.215	5874.60	11.7 ± 0.6	5885.53	11.4 ± 0.5	5931.16	10.6 ± 0.5
5978.93	Si II	4	-0.231	—	—	5988.92	0.06 ± 0.01	—	—
6046.23	O I	22	-0.242	—	—	6056.45	0.05 ± 0.01	—	—
6046.44	O I	22	—	—	—	—	—	—	—
6046.49	O I	22	—	—	—	—	—	—	—
6300.30	[O I]	1F	-0.282	6299.10	1.06 ± 0.06	6310.84	1.69 ± 0.09	6359.80	3.0 ± 0.2
6312.10	[S III]	3F	-0.283	6310.93	2.1 ± 0.1	6322.66	1.72 ± 0.09	6371.70	1.44 ± 0.09
6347.11	Si II	4	-0.289	6345.90	0.05:	6357.72	0.06 ± 0.01	—	—
6363.78	[O I]	1F	-0.291	6362.61	0.32 ± 0.02	6374.40	0.56 ± 0.04	6423.91	0.92 ± 0.07
6371.36	Si II	2	-0.292	6370.21	0.06:	—	—	—	—
6548.03	[N II]	1F	-0.318	6546.84	1.7 ± 0.1	6559.02	1.00 ± 0.06	6609.97	1.9 ± 0.1
6562.82	H I	H α	-0.320	6561.61	284 ± 17	6573.84	283 ± 14	6624.79	279 ± 14
6578.05	C II	2	-0.322	6576.82	0.05:	—	—	—	—
6583.41	[N II]	1F	-0.323	6582.20	5.5 ± 0.3	6594.47	3.3 ± 0.2	6645.66	5.8 ± 0.3
6678.15	He I	46	-0.336	6676.95	3.5 ± 0.2	6689.33	3.4 ± 0.2	6741.25	3.0 ± 0.2
6716.47	[S II]	2F	-0.342	6715.21	7.8 ± 0.5	6727.69	7.3 ± 0.4	6779.92	10.8 ± 0.6
6730.85	[S II]	2F	-0.344	6729.59	5.9 ± 0.4	6742.09	6.0 ± 0.3	6794.43	8.2 ± 0.4
7065.28	He I	10	-0.387	7063.97	2.9 ± 0.2	7077.09	4.4 ± 0.2	7131.90	3.3 ± 0.2
7135.78	[Ar III]	1F	-0.396	7134.51	10.8 ± 0.7	7147.75	7.4 ± 0.4	7203.18	6.7 ± 0.4
7254.15	O I	20	-0.411	—	—	—	—	7322.78	0.07 ± 0.02
7254.45	O I	20	—	—	—	—	—	—	—
7254.53	O I	20	—	—	—	—	—	—	—
7281.35	He I	45	-0.414	7280.05	0.66 ± 0.05	7293.56	0.68 ± 0.04	7350.11	0.60 ± 0.05
7318.39	[O II]	2F	-0.418	7317.73	0.38 ± 0.03	7331.28	0.46 ± 0.03	7389.04	2.3 ± 0.2
7319.99	[O II]	2F	-0.418	7318.75	1.5 ± 0.1	7332.34	1.33 ± 0.08	—	—
7329.66	[O II]	2F	-0.420	7328.32	0.83 ± 0.06	7341.92	0.64 ± 0.04	7399.43	1.8 ± 0.1
7330.73	[O II]	2F	-0.420	7329.39	0.76 ± 0.06	7342.97	0.75 ± 0.05	—	—
7377.83	[Ni II]	2F	-0.425	—	—	7390.18	0.062 ± 0.008	7447.54	0.13 ± 0.02
7442.3	N I	3	-0.433	—	—	—	—	7512.60	0.07 ± 0.02
7468.31	N I	3	-0.436	—	—	—	—	7538.65	0.11 ± 0.02
7499.85	He I	1/8	-0.439	7498.53	0.040 ± 0.006	7512.43	0.046 ± 0.007	—	—
7530.54	[Cl IV]	1F	-0.443	7529.05	0.059 ± 0.008	7543.10	0.09 ± 0.01	—	—
7530.57	C II	16.8	—	—	—	—	—	—	—
7751.10	[Ar III]	2F	-0.467	7749.76	2.9 ± 0.2	7764.11	1.8 ± 0.1	7824.33	1.6 ± 0.1
8045.62	[Cl IV]	1F	-0.497	8044.40	0.073 ± 0.009	8059.31	0.21 ± 0.02	8121.46	0.14 ± 0.02
8188.01	N I	2	-0.510	—	—	8201.69	0.054 ± 0.008	—	—
8216.34	N I	2	-0.513	8214.75	0.043 ± 0.006	8230.12	0.054 ± 0.008	—	—
8223.14	N I	2	-0.514	8221.61	0.041 ± 0.006	8236.87	0.066 ± 0.009	—	—
8247.73	H I	P41	-0.516	8246.23	0.035 ± 0.006	—	—	—	—
8249.2	H I	P40	-0.516	8248.48	0.081 ± 0.009	—	—	—	—
8252.4	H I	P39	-0.516	8250.93	0.044 ± 0.006	—	—	—	—
8255.02	H I	P38	-0.517	8253.54	0.033 ± 0.005	—	—	—	—
8257.85	H I	P37	-0.517	8256.18	0.066 ± 0.008	—	—	—	—
8260.93	H I	P36	-0.517	8259.46	0.059 ± 0.008	—	—	—	—

Table 2. *continued*

λ_0 (Å)	Ion	ID	$f(\lambda)$	HV (NGC 6822)		NGC 5408		Tot 1924–416	
				λ (Å)	$I(\lambda)$	λ (Å)	$I(\lambda)$	λ (Å)	$I(\lambda)$
8264.28	H I	P35	-0.517	8262.87	0.069 ± 0.008	—	—	—	—
8267.94	H I	P34	-0.518	8266.43	0.061 ± 0.008	—	—	—	—
8271.93	H I	P33	-0.518	8270.48	0.09 ± 0.01	—	—	—	—
8276.31	H I	P32	-0.518	8274.63	0.037 ± 0.006	8290.50	0.09 ± 0.01	—	—
8286.43	H I	P30	-0.519	8284.94	0.09 ± 0.01	—	—	—	—
8292.31	H I	P29	-0.520	8291.13	0.18 ± 0.02	8306.24	0.08 ± 0.01	—	—
8298.83	H I	P28	-0.520	—	—	8312.87	0.09 ± 0.01	—	—
8306.11	H I	P27	-0.521	8304.64	0.12 ± 0.01	8320.02	0.11 ± 0.01	—	—
8314.26	H I	P26	-0.522	8312.83	0.12 ± 0.01	8328.21	0.13 ± 0.01	8392.32	0.15 ± 0.03
8323.42	H I	P25	-0.523	8321.81	0.10 ± 0.01	8337.49	0.19 ± 0.02	—	—
8333.78	H I	P24	-0.524	8332.35	0.22 ± 0.02	8347.87	0.19 ± 0.02	8412.46	0.17 ± 0.03
8345.55	H I	P23	-0.525	—	—	8359.82	0.24 ± 0.02	8424.25	0.19 ± 0.03
8359.00	H I	P22	-0.526	8357.44	0.22 ± 0.02	8373.01	0.22 ± 0.02	8437.83	0.16 ± 0.03
8361.73	He I	1/6	-0.526	8360.24	0.081 ± 0.009	8375.77	0.11 ± 0.01	—	—
8374.48	H I	P21	-0.527	8372.98	0.25 ± 0.02	8388.50	0.25 ± 0.02	—	—
8392.40	H I	P20	-0.529	8390.91	0.34 ± 0.03	8406.43	0.30 ± 0.02	8471.55	0.28 ± 0.04
8413.32	H I	P19	-0.531	8411.81	0.34 ± 0.03	8427.46	0.36 ± 0.03	—	—
8437.96	H I	P18	-0.533	8436.44	0.40 ± 0.04	8452.24	1.15 ± 0.08	8517.54	0.32 ± 0.04
8446.25	O I	4	-0.534	8444.88	0.27 ± 0.03	8460.57	0.60 ± 0.05	8526.16	0.73 ± 0.07
8446.36	O I	4	—	—	—	—	—	—	—
8446.76	O I	4	—	—	—	—	—	—	—
8459.50	Ca I] ?	—	-0.535	8457.73	0.039 ± 0.006	8473.40	0.038 ± 0.007	—	—
8467.25	H I	P17	-0.536	—	—	8481.46	0.44 ± 0.03	—	—
8502.48	H I	P16	-0.539	8500.99	0.56 ± 0.05	8516.75	0.52 ± 0.04	—	—
8598.39	H I	P14	-0.547	—	—	—	—	8679.47	0.65 ± 0.06
8665.02	H I	P13	-0.553	8663.46	0.98 ± 0.09	8679.66	1.09 ± 0.08	8746.87	0.82 ± 0.07
8727.13	[C I] ?	—	-0.558	8725.56	0.021 ± 0.004	—	—	—	—
8733.43	He I	6/12	-0.558	8731.88	0.037 ± 0.006	—	—	—	—
8750.47	H I	P12	-0.560	8748.91	1.2 ± 0.1	8765.13	1.14 ± 0.09	8833.25	1.6 ± 0.1
8845.38	He I	6/11	-0.567	8843.79	0.045 ± 0.006	—	—	—	—
8862.79	H I	P11	-0.569	8861.21	1.6 ± 0.1	8877.66	1.5 ± 0.1	8946.45	1.4 ± 0.1
8996.99	He I	6/10	-0.579	8995.37	0.065 ± 0.008	—	—	—	—
9014.91	H I	P10	-0.581	9013.35	1.9 ± 0.2	9030.05	2.0 ± 0.2	9099.91	1.5 ± 0.1
9063.32	He I	4/8	-0.584	9061.81	0.056 ± 0.007	—	—	—	—
9068.90	[S III]	1F	-0.585	9067.32	23 ± 2	9084.14	14 ± 1	9154.62	13 ± 1
9213.24	He I	7/9	-0.595	9211.56	0.037 ± 0.006	—	—	—	—
9229.01	H I	P9	-0.596	9227.36	3.0 ± 0.3	9244.51	2.6 ± 0.2	—	—
9516.57	He I	4/7	-0.617	9514.95	0.058 ± 0.008	9532.40	0.13 ± 0.01	—	—
9526.17	He I	6/8	-0.617	9524.53	0.12 ± 0.01	—	—	—	—
9530.60	[S III]	1F	-0.618	9529.21	29 ± 3	9546.97	31 ± 2	9621.01	34 ± 3
9545.97	H I	P8	-0.619	9544.13	2.7 ± 0.3	9561.92	3.6 ± 0.3	9635.97	3.6 ± 0.3
10031.2	He I	7/7	-0.649	10029.53	0.08 ± 0.01	—	—	—	—
10049.40	H I	P7	-0.650	10047.59	6.8 ± 0.7	10066.30	6.7 ± 0.6	10144.22	6.2 ± 0.5
$c(\text{H}\beta)$	—	—	—	0.54 ± 0.06	—	0.25 ± 0.05	—	0.26 ± 0.05	—
$F(\text{H}\beta)$ (10^{-13} erg cm $^{-2}$ s $^{-1}$)	—	—	—	2.9 ± 0.1	—	4.3 ± 0.2	—	2.8 ± 0.1	—
$-W(\text{H}\beta)$ (Å)	—	—	—	279	—	195	—	132	—
W_{abs} (Å)	—	—	—	2.5	—	0.9	—	1.0	—

^a Blend of [O II] λ 7318.39 and λ 7319.99 lines.^b Blend of [O II] λ 7329.66 and λ 7330.73 lines.

outlined by López-Sánchez et al. (2006). We have used the reddening curve of Cardelli et al. (1989) –assuming $R_V = 3.1$ – and the observed $\text{H}\alpha/\text{H}\beta$, $\text{H}\gamma/\text{H}\beta$, $\text{H}\delta/\text{H}\beta$, and $\text{H}\epsilon/\text{H}\beta$ line ratios. We have considered the theoretical line ratios expected for case B recombination given by Storey & Hummer (1995) for electron densities of 100 cm^{-3} and a first estimation of the electron temperature of each object based on the line intensity ratios not corrected for reddening. At the end of tables 2, 3 and 4, we include the $c(\text{H}\beta)$ and W_{abs} pairs that

provide the best match between the corrected and the theoretical line ratios. In the tables we also include the observed –uncorrected for reddening– integrated $\text{H}\beta$ flux, $F(\text{H}\beta)$ and the equivalent width of this line, $W(\text{H}\beta)$.

Tables 2, 3, and 4 show all the emission-line intensities measured and provide the most complete collection of emission lines available for the sample objects. For comparison, while Guseva et al. (2011) –using the same dataset– give line intensity ratios for 46 and 45 lines for NGC 5408 and HV

Table 3. Dereddened line intensity ratios with respect to $I(\text{H}\beta) = 100$ of Mkn 3125, Mkn 1271, and POX 4.

λ_0 (Å)	Ion	ID	$f(\lambda)$	NGC 3125		Mkn 1271		POX 4	
				λ (Å)	$I(\lambda)$	λ (Å)	$I(\lambda)$	λ (Å)	$I(\lambda)$
3187.84	He I	3	0.308	3199.36	1.0 ± 0.1	3198.69	1.0 ± 0.2	3225.32	1.3 ± 0.2
3447.59	He I	7	0.295	3460.10	0.3 ± 0.1	—	—	—	—
3587.28	He I	3	0.278	3600.45	0.4 ± 0.1	—	—	—	—
3613.64	He I	6	0.275	3626.81	0.3 ± 0.1	—	—	—	—
3634.25	He I	28	0.272	3647.34	0.3 ± 0.1	—	—	3677.03	0.3 ± 0.1
3669.47	H I	H25	0.266	3682.93	0.3 ± 0.1	—	—	—	—
3671.48	H I	H24	0.266	3684.79	0.4 ± 0.1	—	—	—	—
3673.76	H I	H23	0.265	3687.09	0.5 ± 0.1	—	—	—	—
3676.37	H I	H22	0.265	3689.64	0.6 ± 0.1	3688.95	0.3 ± 0.1	—	—
3679.36	H I	H21	0.265	3692.72	0.6 ± 0.1	3692.01	0.5 ± 0.1	3722.68	0.6 ± 0.1
3682.81	H I	H20	0.264	3696.18	0.7 ± 0.1	3695.38	0.7 ± 0.1	3726.17	0.9 ± 0.1
3686.83	H I	H19	0.263	3700.23	0.9 ± 0.1	3699.48	0.7 ± 0.1	3730.18	0.7 ± 0.1
3691.56	H I	H18	0.263	3705.00	0.9 ± 0.1	3704.20	1.0 ± 0.2	3735.02	0.9 ± 0.1
3697.15	H I	H17	0.262	3710.57	1.2 ± 0.1	3709.85	1.0 ± 0.2	3740.72	1.2 ± 0.2
3703.86	H I	H16	0.260	3717.58	1.9 ± 0.2	3716.54	1.0 ± 0.2	3747.44	1.2 ± 0.2
3705.04	He I	25	0.260	—	—	—	—	3748.54	0.6 ± 0.1
3711.97	H I	H15	0.259	3725.68	2.1 ± 0.2	3724.68	1.3 ± 0.2	3755.64	1.7 ± 0.2
3721.83	[S III]	2F	0.257	3735.39	2.7 ± 0.2	3734.56	2.7 ± 0.3	3765.64	3.2 ± 0.3
3721.94	H I	H14	—	—	—	—	—	—	—
3726.03	[O II]	1F	0.257	3739.62	67 ± 4	3738.73	61 ± 3	3769.88	41 ± 2
3728.82	[O II]	1F	0.256	3742.39	87 ± 5	3741.49	77 ± 4	3772.66	54 ± 2
3734.37	H I	H13	0.255	3747.95	1.9 ± 0.2	3747.10	2.2 ± 0.2	3778.30	2.3 ± 0.1
3750.15	H I	H12	0.253	3763.79	2.9 ± 0.2	3762.99	2.7 ± 0.2	3794.28	2.8 ± 0.2
3770.63	H I	H11	0.249	3784.34	3.6 ± 0.2	3783.53	3.3 ± 0.2	3814.99	3.5 ± 0.2
3797.90	H I	H10	0.244	3811.71	5.0 ± 0.3	3810.89	4.7 ± 0.3	3842.58	4.7 ± 0.2
3816.7	Ne II ?	—	0.240	3830.54	0.07 ± 0.02	—	—	—	—
3819.61	He I	22	0.240	3833.49	0.92 ± 0.07	3832.65	0.91 ± 0.09	3864.55	0.79 ± 0.07
3835.39	H I	H9	0.237	3849.33	6.8 ± 0.4	3848.50	6.8 ± 0.4	3880.51	6.9 ± 0.3
3868.75	[Ne III]	1F	0.230	3882.81	37 ± 2	3882.01	53 ± 3	3914.29	50 ± 2
3889.05	H I	H8	0.226	3903.01	19 ± 1	3902.16	18 ± 1	3934.66	17.3 ± 0.8
3964.73	He I	5	0.211	3979.16	0.60 ± 0.06	3978.33	0.65 ± 0.08	4011.34	0.55 ± 0.06
3967.46	[Ne III]	1F	0.211	3981.87	10.7 ± 0.5	3981.06	15.4 ± 0.8	4014.12	14.3 ± 0.6
3970.07	H I	H7	0.210	3984.51	15.1 ± 0.8	3983.66	14.9 ± 0.8	4016.77	15.0 ± 0.6
4009.22	He I	55	0.202	4023.76	0.20 ± 0.03	—	—	—	—
4026.21	He I	18	0.198	4040.88	1.9 ± 0.1	4040.02	1.7 ± 0.1	4073.61	1.7 ± 0.1
4068.60	[S II]	1F	0.189	4083.46	1.27 ± 0.09	4082.46	1.2 ± 0.1	4116.49	0.95 ± 0.07
4076.35	[S II]	1F	0.187	4091.11	0.37 ± 0.04	4090.24	0.24 ± 0.05	4124.28	0.32 ± 0.05
4087.15	O II	48	0.185	4101.89	0.14 ± 0.03	—	—	—	—
4101.74	H I	H6	0.182	4116.64	26 ± 1	4115.76	25 ± 1	4150.00	25 ± 1
4120.82	He I	16	0.177	4135.73	0.17 ± 0.03	4134.99	0.17 ± 0.05	4169.27	0.14 ± 0.04
4143.76	He I	53	0.172	—	—	4158.03	0.16 ± 0.05	4192.48	0.18 ± 0.04
4243.97	[Fe II]	21F	0.149	—	—	4258.78	0.11 ± 0.04	—	—
4267.15	C II	6	0.144	4282.22	0.11:	4281.34	0.07:	4317.13	0.10:
4287.40	[Fe II]	7F	0.139	4302.99	0.18 ± 0.03	4301.83	0.13 ± 0.04	4337.86	0.11 ± 0.04
4324.79	O II ?	—	0.130	4340.41	0.18 ± 0.03	—	—	—	—
4340.47	H I	H γ	0.127	4356.24	47 ± 2	4355.31	46 ± 2	4391.54	47 ± 2
4363.21	[O III]	2F	0.121	4379.04	3.7 ± 0.2	4378.15	9.3 ± 0.4	4414.56	9.9 ± 0.4
4387.93	He I	51	0.115	4403.88	0.40 ± 0.04	4402.99	0.48 ± 0.07	4439.49	0.39 ± 0.05
4413.78	[Fe II]	7F	0.109	—	—	—	—	4465.75	0.06:
4452.11	[Fe II]	7F	0.100	—	—	—	—	4504.49	0.09 ± 0.03
4471.48	He I	14	0.096	4487.76	3.9 ± 0.2	4486.81	3.7 ± 0.2	4524.13	3.8 ± 0.2
4562.60	[Mg I]	—	0.073	4579.07	0.24 ± 0.03	4578.04	0.27 ± 0.05	4616.27	0.19 ± 0.04
4571.10	Mg I	—	0.071	4587.64	0.15 ± 0.03	—	—	4624.83	0.14 ± 0.04
4638.86	O II	1	0.055	4655.60	0.06 ± 0.02	4657.73	0.18 ± 0.05	—	—
4641.81	O II	1	0.054	4658.76	0.15 ± 0.03	4660.00	0.11 ± 0.04	—	—
4649.13	O II	1	0.052	4667.32	0.16 ± 0.03	4665.20	0.09:	—	—
4650.84	O II	1	0.052	—	—	4666.65	0.08:	4705.72	0.04:
4658.10	[Fe III]	3F	0.050	4675.10	0.62 ± 0.05	4674.15	0.65 ± 0.07	4712.87	0.58 ± 0.06
4661.63	O II	1	0.049	—	—	4680.95	0.09:	—	—
4667.01	[Fe III]	3F	0.048	4682.32	0.05 ± 0.02	—	—	—	—
4685.71	He II	—	0.043	—	—	4701.50	0.30 ± 0.05	4740.83	1.13 ± 0.07
4701.53	[Fe III]	3F	0.039	4718.65	0.16 ± 0.03	—	—	4756.74	0.26 ± 0.04

Table 3. *continued*

λ_0 (Å)	Ion	ID	$f(\lambda)$	NGC 3125		Mkn 1271		POX 4	
				λ (Å)	$I(\lambda)$	λ (Å)	$I(\lambda)$	λ (Å)	$I(\lambda)$
4708.04	?		0.038	4725.11	0.03 ± 0.01	—	—	—	—
4711.37	[Ar IV]	1F	0.037	4728.48	0.37 ± 0.04	4727.54	1.03 ± 0.09	4766.80	1.10 ± 0.07
4713.14	He I	12	0.036	4730.27	0.48 ± 0.04	4729.30	0.54 ± 0.07	4768.51	0.56 ± 0.05
4740.16	[Ar IV]	1F	0.030	4757.40	0.27 ± 0.03	4756.45	0.76 ± 0.08	4796.02	0.98 ± 0.07
4754.83	[Fe III]	3F	0.026	4771.95	0.11 ± 0.02	—	—	—	—
4777.88	[Fe III]	3F	0.021	4794.86	0.04 ± 0.02	—	—	—	—
4861.33	H I	H β	0.000	4879.00	100 ± 4	4877.96	100 ± 4	4918.53	100 ± 4
4881	[Fe III]	2F	-0.005	4898.38	0.28 ± 0.03	—	—	—	—
4906.56	[Fe IV]		-0.011	4924.26	0.16 ± 0.03	—	—	—	—
4921.93	He I	48	-0.015	4939.83	1.00 ± 0.06	4938.82	0.91 ± 0.08	4979.89	0.95 ± 0.09
4958.91	[O III]	1F	-0.024	4976.95	179 ± 7	4975.92	202 ± 8	5017.35	227 ± 8
4985.9	[Fe III]	2F	-0.031	5004.01	0.62 ± 0.08	5002.93	0.49 ± 0.05	5044.48	0.87 ± 0.09
5006.84	[O III]	1F	-0.036	5025.04	514 ± 21	5024.02	642 ± 26	5065.85	695 ± 24
5015.68	He I	4	-0.038	5033.91	2.0 ± 0.1	5032.90	1.9 ± 0.1	5074.74	2.0 ± 0.1
5047.74	He I	47	-0.046	—	—	—	—	5107.90	0.81 ± 0.09
5158.81	[Fe II]	19F	-0.091	—	—	—	—	5219.36	0.05:
5197.90	[N I]	1F	-0.082	5216.82	0.50 ± 0.07	5215.75	0.14 ± 0.03	5259.14	0.26 ± 0.06
5200.26	[N I]	1F	-0.083	5219.25	0.30 ± 0.06	5218.12	0.04:	5261.49	0.09:
5517.71	[Cl III]	1F	-0.154	5537.84	0.37 ± 0.06	5536.63	0.32 ± 0.04	5582.73	0.30 ± 0.06
5537.88	[Cl III]	1F	-0.158	5557.99	0.27 ± 0.06	5556.70	0.21 ± 0.03	5603.04	0.20 ± 0.05
5875.64	He I	11	-0.215	5897.09	10.8 ± 0.6	5895.63	12.6 ± 0.7	5944.88	10.9 ± 0.5
6300.30	[O I]	1F	-0.282	6323.19	2.6 ± 0.2	6321.66	4.3 ± 0.3	6374.51	2.2 ± 0.1
6312.10	[S III]	3F	-0.283	6334.97	1.5 ± 0.1	6333.67	1.6 ± 0.1	6386.43	2.1 ± 0.1
6363.78	[O I]	1F	-0.291	6386.79	1.02 ± 0.09	6385.63	1.2 ± 0.1	6438.74	0.66 ± 0.08
6548.03	[N II]	1F	-0.318	6571.89	4.1 ± 0.3	6570.42	2.2 ± 0.2	6625.17	1.3 ± 0.1
6562.82	H I	H α	-0.320	6586.63	291 ± 17	6585.26	282 ± 17	6640.11	283 ± 14
6583.41	[N II]	1F	-0.323	6607.38	13.0 ± 0.8	6605.89	7.3 ± 0.5	6660.96	4.4 ± 0.3
6678.15	He I	46	-0.336	6702.48	3.2 ± 0.2	6701.01	3.4 ± 0.2	6756.81	2.9 ± 0.2
6716.47	[S II]	2F	-0.342	6740.88	14.0 ± 0.9	6739.38	14.4 ± 0.9	6795.56	8.9 ± 0.5
6730.85	[S II]	2F	-0.344	6755.30	10.8 ± 0.7	6753.80	11.3 ± 0.7	6810.10	6.3 ± 0.3
7065.28	He I	10	-0.387	7090.89	2.7 ± 0.2	7089.43	3.2 ± 0.2	7148.37	2.6 ± 0.2
7135.78	[Ar III]	1F	-0.396	7161.71	8.8 ± 0.6	7160.24	7.8 ± 0.5	7219.76	6.8 ± 0.4
7281.35	He I	45	-0.414	7307.65	0.52 ± 0.05	—	—	7366.97	0.49 ± 0.04
7318.39	[O II]	2F	-0.418	7346.45	1.9 ± 0.1	7344.91	2.0 ± 0.2	7406.00	1.4 ± 0.1
7319.99	[O II]	2F	-0.418	—	—	—	—	—	—
7329.66	[O II]	2F	-0.420	7356.75	1.5 ± 0.1	7355.20	1.5 ± 0.1	7416.45	1.20 ± 0.08
7330.73	[O II]	2F	-0.420	7358.18	0.81 ± 0.07	—	—	—	—
7751.10	[Ar III]	2F	-0.467	7778.92	1.4 ± 0.1	7777.72	1.7 ± 0.1	7842.32	1.33 ± 0.09
8286.43	H I	P30	-0.519	—	—	—	—	8384.90	0.10 ± 0.02
8314.26	H I	P26	-0.522	—	—	—	—	8412.16	0.14 ± 0.02
8333.78	H I	P24	-0.524	—	—	—	—	8422.18	0.18 ± 0.02
8345.55	H I	P23	-0.525	8375.77	0.13 ± 0.02	—	—	8443.65	0.09 ± 0.02
8359.00	H I	P22	-0.526	8389.87	0.33 ± 0.04	—	—	8457.25	0.13 ± 0.02
8361.73	He I	1/6	-0.526	—	—	—	—	8460.30	0.08 ± 0.01
8374.48	H I	P21	-0.527	8404.90	0.23 ± 0.03	8403.20	0.24 ± 0.03	8472.86	0.18 ± 0.02
8376.56	He I	6/20	-0.528	—	—	—	—	8474.16	0.18 ± 0.02
8392.40	H I	P20	-0.529	8422.95	0.34 ± 0.04	8421.77	0.31 ± 0.04	8490.98	0.21 ± 0.02
8413.32	H I	P19	-0.531	8444.30	0.30 ± 0.04	8442.16	0.12 ± 0.02	8512.39	0.21 ± 0.02
8437.96	H I	P18	-0.533	8468.63	0.27 ± 0.03	8466.90	0.24 ± 0.03	—	—
8446.25	O I	4	-0.534	8477.00	0.52 ± 0.05	8475.45	0.32 ± 0.04	—	—
8446.36	O I	4	—	—	—	—	—	—	—
8446.76	O I	4	—	—	—	—	—	—	—
8467.25	H I	P17	-0.536	8497.81	0.35 ± 0.04	8496.21	0.21 ± 0.03	—	—
8598.39	H I	P14	-0.547	—	—	—	—	8699.64	0.78 ± 0.06
8665.02	H I	P13	-0.553	8696.57	0.73 ± 0.07	8694.93	0.63 ± 0.06	—	—
8750.47	H I	P12	-0.560	8782.23	1.1 ± 0.1	8780.47	1.1 ± 0.1	8853.50	0.99 ± 0.08
8862.79	H I	P11	-0.569	8895.02	1.4 ± 0.1	8893.28	1.2 ± 0.1	8967.16	1.2 ± 0.1
9014.91	H I	P10	-0.581	9047.31	1.1 ± 0.1	9045.76	1.6 ± 0.2	9121.02	1.5 ± 0.1
9015.77	N II ?		-0.581	9048.89	2.1 ± 0.2	—	—	—	—
9068.90	[S III]	1F	-0.585	9101.91	20 ± 2	9100.31	14 ± 1	9175.70	13 ± 1
9229.01	H I	P9	-0.596	9262.53	2.5 ± 0.2	9260.81	2.2 ± 0.2	—	—
9530.60	[S III]	1F	-0.618	9565.77	40 ± 4	9563.58	25 ± 2	9643.07	32 ± 3

Table 3. *continued*

λ_0 (Å)	Ion	ID	$f(\lambda)$	NGC 3125		Mkn 1271		POX 4	
				λ (Å)	$I(\lambda)$	λ (Å)	$I(\lambda)$	λ (Å)	$I(\lambda)$
9545.97	H I	P8	-0.619	9581.4	1.3 ± 0.1	—	—	9658.32	3.4 ± 0.3
10049.40	H I	P7	-0.650	—	—	—	—	10167.5	5.6 ± 0.5
$c(H\beta)$				0.45 ± 0.06		0.10 ± 0.06		0.20 ± 0.05	
$F(H\beta)$ (10^{-13} erg cm $^{-2}$ s $^{-1}$)				1.78 ± 0.07		1.43 ± 0.06		2.6 ± 0.1	
$-W(H\beta)$ (Å)				78		88		148	
W_{abs} (Å)				0.5		1.2		1.5	

^a Blend of [O II] λ 7318.39 and λ 7319.99 lines.

^b Blend of [O II] λ 7329.66 and λ 7330.73 lines.

(NGC 6822), respectively, we identify and measure 177 and 166 lines in these two objects. Our list of identified emission lines is also more complete for the rest of the objects. Columns 1 to 3 of the tables give the laboratory wavelength and the identification –ion and multiplet– of each line. Column 4 indicates the $f(\lambda)$ value of the extinction curve for each line. Columns 5, 7, and 9 give the observed wavelength of the lines –corrected for heliocentric velocity– measured in each of the 3 objects included in each table. Finally, columns 6, 8, and 10 give the dereddened intensity line ratios with respect to H β and their associated uncertainty. The quoted errors include the uncertainties in line intensity measurement and error propagation in the reddening coefficient.

As an example, Figure 2 plots sections of our flux-calibrated echelle spectra showing the recombination lines of C II 4267 Å and multiplet 1 of O II around 4650 Å in the case of HV (NGC 6822) and NGC 5408.

4 RESULTS

4.1 Physical Conditions

Physical conditions were calculated from emission-line ratios of CELs with PYNEB (Luridiana et al. 2012), an updated PYTHON version of the NEBULAR package of IRAF, in combination with the atomic data listed in Table 5. Electron temperature and density, T_e and n_e , were determined making use of the diagnostic ratios available in our spectrum that were numerous due to their long exposure times and wide spectral coverage. Electron densities have been derived from [N I] 5198/5200, [O II] 3726/3729, [S II] 6717/6731, [Cl III] 5518/5538, [Ar IV] 4711/4740, and the ratios of several [Fe III] lines. Electron temperatures have been calculated using several sets of auroral to nebular line intensity ratios: [N II] 5755/(6548+6584), [O II] (7319+7330)/(3726+3729), [S II] (4069+4076)/(6717+6731), [O III] 4363/(4959+5007), [S III] 6312/(9069+9532), and [Ar III] 5192/(7136+7751). T_e ([O II]) and T_e ([N II]) have been corrected from the contribution to the intensity of [O II] 7319, 7330 Å and [N II] 5755 Å lines due to recombination following the formulae derived by Liu et al. (2000). The physical conditions are presented in Table 6. All the objects show low values of n_e , in the range between 100 and 200 cm $^{-3}$ except in the case of He 2–10, where the densities are between 500 and 2000 cm $^{-3}$. In some objects, the n_e derived from [Fe III], [Cl III], or [Ar IV] show values larger than the other diagnostics, in-

dicating possible density structure. Following Ferland et al. (2012), the intensity of [N I] lines are affected by pumping by far-ultraviolet stellar radiation and therefore the high value of n_e determined from those lines in the case of HV (NGC 6822) may be incorrect. In general, our n_e values agree with those derived by Guseva et al. (2011) and other authors for the same objects. In the case of T_e we want to remark the high consistency of the values we obtain from the different indicators for the same objects. The values of T_e indicated in Table 6 are also in general consistent with those obtained by other authors but there are some discrepancies. The T_e ([S II]) derived by Guseva et al. (2011) for He 2–10, Mrk 1271, NGC 3125, NGC 5408, HV (NGC 6822), and Tol 1924–416 are several thousands K lower than the values we obtain, being our determinations much more consistent with T_e ([O II]). This may be due to the use of different sets of atomic data for S $^+$. There are also large differences in the values of T_e ([O II]) that Guseva et al. (2011) and us obtain for NGC 5408 and SDSS J1253–0312, being our values much larger but also more consistent with the temperatures obtained for other ions. In contrast, we obtain a much larger T_e ([S III]) for POX 4, and this value is clearly inconsistent with the temperatures of the rest of ions. We assume a two-zone approximation for the nebula estimating the representative values of the electron temperature for the zones where low and high-ionization potential ions are present, T (low) and T (high). Those values will be used for determining ionic abundances. T (low) is calculated as the mean of T_e ([N II]), T_e ([O II]) and T_e ([S II]) weighted by their inverse relative errors. The same procedure has been used to derive T (high) from T_e ([O III]), T_e ([S III]) and T_e ([Ar III]), except in the case of POX 4, where its abnormal high T_e ([S III]) has not been considered. These temperatures are included in Table 6. It must be advised that very recent calculations by Storey et al. (2014) find rather different values of the collision strengths for CELs of O $^{2+}$ with respect to those calculated by Palay et al. (2012) – the dataset that we have used in our calculations for that ion. Using the collision strengths of Storey et al. (2014) – the previous collision strengths calculated by Aggarwal & Keenan (1999) give very similar T_e ([O III]) values – would imply values of T_e ([O III]) of the order of 400-500 K higher than the ones we give in Table 6.

Table 4. Dereddened line intensity ratios with respect to $I(\text{H}\beta) = 100$ of SDSS J1253–0312, Tol 1457–262, and He 2–10.

λ_0 (Å)	Ion	ID	$f(\lambda)$	SDSS J1253–0312		Tol 1457–262		He 2–10	
				λ (Å)	$I(\lambda)$	λ (Å)	$I(\lambda)$	λ (Å)	$I(\lambda)$
3187.84	He I	3	0.308	3260.20	5.4 ± 0.4	3241.72	2.1 ± 0.4	3197.1	0.7 ± 0.1
3671.48	H I	H24	0.266	–	–	–	–	3682.3	0.30 ± 0.09
3673.76	H I	H23	0.265	–	–	–	–	3684.3	0.4 ± 0.1
3676.37	H I	H22	0.265	3759.86	0.4 ± 0.1	–	–	3686.9	0.5 ± 0.1
3679.36	H I	H21	0.265	3762.91	0.4 ± 0.1	–	–	3690.0	0.5 ± 0.1
3682.81	H I	H20	0.264	3766.56	0.5 ± 0.1	–	–	3693.5	0.6 ± 0.1
3686.83	H I	H19	0.263	3770.70	0.7 ± 0.1	–	–	3697.5	0.6 ± 0.1
3691.56	H I	H18	0.263	3775.42	0.8 ± 0.1	3754.14	1.0 ± 0.2	3702.2	0.8 ± 0.1
3697.15	H I	H17	0.262	3781.16	1.1 ± 0.2	3759.59	1.3 ± 0.1	3707.8	0.9 ± 0.1
3703.86	H I	H16	0.260	3788.36	1.6 ± 0.2	3766.60	1.8 ± 0.2	3714.6	0.6 ± 0.1
3711.97	H I	H15	0.259	3796.30	1.4 ± 0.2	3774.67	1.6 ± 0.2	3722.7	0.8 ± 0.1
3721.83	[S III]	2F	0.257	3806.38	1.3 ± 0.2	3784.75	2.7 ± 0.2	3726.4	0.5 ± 0.1
3721.94	H I	H14	–	–	–	–	–	–	–
3726.03	[O II]	1F	0.257	3810.81	36 ± 2	3789.04	79 ± 4	3736.9	117 ± 5
3728.82	[O II]	1F	0.256	3813.60	43 ± 2	3791.85	99 ± 5	3739.6	98 ± 5
3734.37	H I	H13	0.255	3819.24	1.7 ± 0.2	3797.45	1.9 ± 0.2	3745.2	1.0 ± 0.1
3750.15	H I	H12	0.253	3835.35	2.7 ± 0.2	3813.55	2.7 ± 0.2	3761.0	1.4 ± 0.1
3770.63	H I	H11	0.249	3856.33	3.5 ± 0.3	3834.36	3.5 ± 0.2	3781.5	1.9 ± 0.1
3797.90	H I	H10	0.244	3884.19	4.7 ± 0.3	3862.08	4.5 ± 0.3	3808.9	2.7 ± 0.2
3819.61	He I	22	0.240	3906.36	1.1 ± 0.1	3884.11	0.8 ± 0.1	–	–
3835.39	H I	H9	0.237	3922.55	6.7 ± 0.4	3900.22	6.8 ± 0.3	3846.5	4.8 ± 0.2
3868.75	[Ne III]	1F	0.230	3956.67	50 ± 3	3934.33	34 ± 1	3879.9	4.8 ± 0.2
3889.05	H I	H8	0.226	3977.27	17.8 ± 0.9	3954.62	17.9 ± 0.8	3900.1	13.3 ± 0.6
3967.46	[Ne III]	1F	0.211	4057.65	15.3 ± 0.8	4034.67	12.6 ± 0.6	–	–
3970.07	H I	H7	0.210	4060.33	14.6 ± 0.8	4037.29	13.6 ± 0.6	3981.5	12.2 ± 0.5
4008.36	[Fe III]	4F	0.202	4099.86	0.19 ± 0.04	4076.27	0.3 ± 0.1	–	–
4026.21	He I	18	0.198	4117.71	1.6 ± 0.1	4094.25	1.4 ± 0.1	4038.0	0.80 ± 0.08
4068.60	[S II]	1F	0.189	4161.17	1.2 ± 0.1	4137.33	1.7 ± 0.1	4080.4	1.4 ± 0.1
4076.35	[S II]	1F	0.187	4168.93	0.40 ± 0.05	4145.20	0.5 ± 0.1	4088.2	0.26 ± 0.06
4101.74	H I	H6	0.182	4194.95	28 ± 1	4171.09	26 ± 1	4113.6	21.3 ± 0.9
4120.82	He I	16	0.177	4214.68	0.24 ± 0.04	–	–	–	–
4143.76	He I	53	0.172	4237.76	0.22 ± 0.04	–	–	–	–
4243.97	[Fe II]	21F	0.149	4340.86	0.09 ± 0.03	–	–	–	–
4267.15	C II	6	0.144	4364.11	0.04:	–	–	–	–
4287.40	[Fe II]	7F	0.139	4384.96	0.14 ± 0.03	4359.68	0.5 ± 0.1	4299.7	0.26 ± 0.06
4340.47	H I	H γ	0.127	4439.11	45 ± 2	4413.87	46 ± 2	4353.0	44 ± 2
4363.21	[O III]	2F	0.121	4462.35	9.7 ± 0.5	4437.01	5.2 ± 0.2	4376.0	0.40 ± 0.06
4387.93	He I	51	0.115	4487.57	0.35 ± 0.05	4462.08	0.34 ± 0.09	–	–
4413.78	[Fe II]	7F	0.109	4513.95	0.10 ± 0.03	4488.13	0.23 ± 0.08	–	–
4416.27	[Fe II]	6F	0.109	4516.55	0.07 ± 0.02	–	–	–	–
4437.55	He I	50	0.104	4538.55	0.09 ± 0.03	–	–	–	–
4452.11	[Fe II]	7F	0.100	4553.46	0.08 ± 0.03	–	–	–	–
4471.48	He I	14	0.096	4573.14	4.0 ± 0.2	4547.16	3.6 ± 0.2	4484.5	2.7 ± 0.1
4562.60	[Mg I]	–	0.073	4666.16	0.18 ± 0.04	–	–	–	–
4571.10	Mg I]	–	0.071	4674.93	0.16 ± 0.03	–	–	–	–
4641.81	O II	1	0.054	4747.54	0.05:	–	–	–	–
4649.13	O II	1	0.052	4755.06	0.04:	–	–	–	–
4658.10	[Fe III]	3F	0.050	4764.11	0.97 ± 0.08	4736.87	1.4 ± 0.1	4671.7	1.59 ± 0.09
4685.71	He II	–	0.043	4792.37	0.66 ± 0.07	4765.01	0.6 ± 0.1	–	–
4701.53	[Fe III]	3F	0.039	4808.58	0.20 ± 0.04	4780.88	0.36 ± 0.09	–	–
4711.37	[Ar IV]	1F	0.037	4818.91	1.6 ± 0.1	4791.88	0.8 ± 0.1	–	–
4740.16	[Ar IV]	1F	0.030	4847.85	0.91 ± 0.08	4820.48	0.43 ± 0.09	–	–
4754.83	[Fe III]	3F	0.026	4862.27	0.14 ± 0.03	4834.77	0.27 ± 0.08	–	–
4861.33	H I	H β	0.000	4971.81	100 ± 4	4943.52	100 ± 4	4875.4	100 ± 4
4881	[Fe III]	2F	-0.005	–	–	4963.33	0.41 ± 0.09	4894.8	0.49 ± 0.06
4921.93	He I	48	-0.015	5033.79	0.68 ± 0.09	5005.16	0.8 ± 0.2	4936.4	0.55 ± 0.06
4958.91	[O III]	1F	-0.024	5071.59	219 ± 9	5042.88	178 ± 6	4973.3	45 ± 2
4985.9	[Fe III]	2F	-0.031	5099.27	0.62 ± 0.09	5069.96	1.7 ± 0.2	–	–
5006.84	[O III]	1F	-0.036	5120.61	647 ± 26	5091.63	532 ± 19	5021.4	135 ± 5
5015.68	He I	4	-0.038	5129.86	0.70 ± 0.09	5100.56	1.7 ± 0.2	5030.3	1.6 ± 0.1
5261.62	[Fe II]	19F	-0.109	–	–	5349.44	0.5 ± 0.1	–	–
5270.40	[Fe III]	1F	-0.111	–	–	5359.31	0.7 ± 0.1	–	–

Table 4. *continued*

λ_0 (Å)	Ion	ID	$f(\lambda)$	SDSS J1253–0312		Tol 1457–262		He 2–10	
				λ (Å)	$I(\lambda)$	λ (Å)	$I(\lambda)$	λ (Å)	$I(\lambda)$
5517.71	[Cl III]	1F	-0.154	5643.20	0.22 ± 0.06	5611.26	0.5 ± 0.1	–	–
5537.88	[Cl III]	1F	-0.158	5663.83	0.18 ± 0.05	5631.95	0.5 ± 0.1	–	–
5875.64	He I	11	-0.215	6009.16	11.6 ± 0.6	5975.12	11.4 ± 0.5	–	–
6300.30	[O I]	1F	-0.282	6443.52	2.3 ± 0.2	6406.79	4.5 ± 0.3	6318.6	1.9 ± 0.1
6312.10	[S III]	3F	-0.283	6455.59	1.6 ± 0.1	6418.97	1.6 ± 0.2	6330.3	0.94 ± 0.07
6347.11	Si II	4	-0.289	–	–	–	–	6365.7	0.20 ± 0.03
6363.78	[O I]	1F	-0.291	6508.41	0.66 ± 0.09	6471.22	1.3 ± 0.1	6382.4	0.52 ± 0.05
6548.03	[N II]	1F	-0.318	6696.85	3.4 ± 0.2	6658.86	3.0 ± 0.2	6567.1	28 ± 1
6562.82	H I	H α	-0.320	6711.93	267 ± 16	6673.83	293 ± 15	6581.9	296 ± 15
6583.41	[N II]	1F	-0.323	6733.13	11.6 ± 0.7	6694.83	9.4 ± 0.5	6602.6	89 ± 5
6678.15	He I	46	-0.336	–	–	6791.10	3.3 ± 0.2	6697.7	2.5 ± 0.1
6716.47	[S II]	2F	-0.342	6869.33	6.3 ± 0.4^a	6829.87	21 ± 1	6735.9	19 ± 1
6730.85	[S II]	2F	-0.344	6883.81	7.9 ± 0.5^a	6844.55	15.8 ± 0.8	6750.3	20 ± 1
7065.28	He I	10	-0.387	7225.80	4.8 ± 0.4	7184.67	2.2 ± 0.1	7085.8	2.5 ± 0.2
7135.78	[Ar III]	1F	-0.396	7297.83	7.5 ± 0.5	7256.52	8.3 ± 0.5	7156.6	6.8 ± 0.4
7281.35	He I	45	-0.414	7446.77	0.56 ± 0.06	7404.55	0.72 ± 0.06	–	–
7318.39	[O II]	2F	-0.418	7486.31 ^b	1.9 ± 0.2	7443.55 ^b	2.6 ± 0.2	7341.0 ^b	3.0 ± 0.2
7319.99	[O II]	2F	-0.418	–	–	–	–	–	–
7329.66	[O II]	2F	-0.420	7496.89 ^c	1.4 ± 0.1	7454.07 ^c	2.1 ± 0.1	7351.7 ^c	1.8 ± 0.1
7330.73	[O II]	2F	-0.420	–	–	–	–	–	–
7377.83	[Ni II]	2F	-0.425	–	–	7502.20	0.37 ± 0.05	–	–
7751.10	[Ar III]	2F	-0.467	7927.28	1.6 ± 0.1	7882.27	2.1 ± 0.1	7773.8	1.4 ± 0.1
8392.40	H I	P20	-0.529	–	–	–	–	8416.6	0.23 ± 0.03
8413.32	H I	P19	-0.531	–	–	–	–	8438.4	0.14 ± 0.02
8437.96	H I	P18	-0.533	–	–	–	–	8462.6	0.16 ± 0.02
8446.25	O I	4	-0.534	–	–	–	–	8471.2	0.59 ± 0.05
8446.36	O I	4	–	–	–	–	–	–	–
8446.76	O I	4	–	–	–	–	–	–	–
8502.48	H I	P16	-0.539	–	–	–	–	8527.5	0.22 ± 0.03
8598.39	H I	P14	-0.547	8793.91	0.71 ± 0.08	8743.67	0.72 ± 0.07	–	–
8665.02	H I	P13	-0.553	8862.05	0.9 ± 0.1	8811.06	0.60 ± 0.06	–	–
8750.47	H I	P12	-0.560	8949.50	0.9 ± 0.1	8898.10	1.09 ± 0.09	–	–
8862.79	H I	P11	-0.569	9064.24	1.1 ± 0.1	9012.71	1.4 ± 0.1	8888.8	0.89 ± 0.07
9014.91	H I	P10	-0.581	9219.98	1.7 ± 0.2	9167.38	1.7 ± 0.1	9041.3	1.3 ± 0.1
9068.90	[S III]	1F	-0.585	9275.03	14 ± 1	9222.42	19 ± 1	9095.5	27 ± 2
9229.01	H I	P9	-0.596	–	–	–	–	9256.0	1.9 ± 0.2
9530.60	[S III]	1F	-0.618	9747.45	36 ± 3	9692.20	48 ± 4	9559.0	63 ± 5
9545.97	H I	P8	-0.619	–	–	9707.25	3.8 ± 0.3	9573.9	2.7 ± 0.2
10049.40	H I	P7	-0.650	–	–	10219.3	5.5 ± 0.5	–	–
$c(\text{H}\beta)$					0.22 ± 0.06		0.45 ± 0.05		0.74 ± 0.05
$F(\text{H}\beta)$ (10^{-13} erg cm $^{-2}$ s $^{-1}$)					2.5 ± 0.1		2.6 ± 0.1		10.5 ± 0.4
$-W(\text{H}\beta)$ (Å)					186		91		39
W_{abs} (Å)					0.0		1.5		1.2

^a Line intensity severely affected by telluric absorption features.

^b Blend of [O II] λ 7318.39 and λ 7319.99 lines.

^c Blend of [O II] λ 7329.66 and λ 7330.73 lines.

Table 5. Atomic dataset used for collisionally excited lines.

Ion	Transition Probabilities	Collisional Strengths
N ⁺	Froese Fischer & Tachiev (2004)	Tayal (2011)
O ⁺	Froese Fischer & Tachiev (2004)	Kisielius et al. (2009)
O ²⁺	Froese Fischer & Tachiev (2004)	Palay et al. (2012)
Ne ²⁺	Froese Fischer & Tachiev (2004)	Aggarwal & Keenan (1999)
S ⁺	Podobedova et al. (2009)	McLaughlin & Bell (2000)
	Tayal & Zatsarinny (2010)	Tayal & Zatsarinny (2010)
S ²⁺	Podobedova et al. (2009)	Galavís et al. (1995)
Ar ²⁺	Mendoza & Zeppen (1983)	Galavís et al. (1995)
Fe ²⁺	Quinet (1996)	Zhang (1996)
	Johansson et al. (2000)	

Table 6. Physical Conditions.

Parameter	Lines	HV (NGC 6822)	NGC 5408	Tol 1924–416	NGC 3125	Mkn 1271
n_e (cm ⁻³)	[N II]	5700:	–	–	–	–
	[S II]	90 ⁺¹¹⁰ ₋₉₀	200 ± 110	90 ⁺¹⁰⁰ ₋₉₀	110 ± 100	130 ± 100
	[O II]	100 ± 70	170 ± 70	100 ± 70	120 ± 80	160 ± 80
	[Fe III]	300 - 2700	250 - 700	130 - 740	10 - 400	200 - 400
	[Cl III]	370 ⁺⁵³⁰ ₋₃₇₀	–	1830 ⁺¹⁹⁶⁰ ₋₁₈₃₀	210 ⁺¹⁶³⁰ ₋₂₁₀	–
	[Ar IV]	130 ⁺⁷²⁰ ₋₁₃₀	870 ± 570	430 ⁺⁹⁰⁰ ₋₄₃₀	190 ⁺¹²³⁰ ₋₁₉₀	–
T_e (K)	[N II]	11800 ± 1500	12080 ± 1100	–	–	–
	[O II]	12600 ± 480	14000 ± 510	13200 ± 460	11600 ± 440	10900 ± 440
	[S II]	12300 ± 700	14100 ± 820	14400 ± 1000	11850 ± 750	10030 ± 670
	$T(\text{low})$	12470 ± 440	13850 ± 720	13430 ± 620	11650 ± 400	10670 ± 530
	[O III]	11050 ± 240	15300 ± 390	13000 ± 290	9850 ± 200	12660 ± 310
	[S III]	11300 ± 630	15700 ± 950	14300 ± 900	11450 ± 680	14900 ± 1100
	[Ar III]	11600 ± 1450	–	–	–	–
	$T(\text{high})$	11280 ± 630	15360 ± 390	13140 ± 510	10010 ± 530	12890 ± 750
		POX 4	SDSS J1253–0312	Tol 1457–262	He 2–10	
n_e (cm ⁻³)	[S II]	<100	–	80 ± 80	530 ± 150	
	[O II]	120 ± 70	220 ± 100	150 ± 70	700 ± 140	
	[Fe III]	70 - 240	200 - 450	100 - 1100	1400:	
	[Cl III]	–	–	870 ⁺³²⁵⁰ ₋₈₇₀	2100 ⁺⁴²⁰⁰ ₋₂₁₀₀	
	[Ar IV]	1690±950	–	–	–	
T_e (K)	[O II]	11800 ± 420	14920 ± 930	11370 ± 400	8240 ± 220	
	[S II]	–	–	11020 ± 780	7050 ± 310	
	$T(\text{low})$	11800 ± 420	14920 ± 930	11300 ± 380	7940 ± 550	
	[O III]	12580 ± 270	12840 ± 330	10900 ± 220	7700 ± 300	
	[S III]	18500 ± 1400	14420 ± 1100	12180 ± 820	8390 ± 330	
	$T(\text{high})$	12580 ± 270	13000 ± 570	11000 ± 420	8040 ± 420	

Table 7. Ionic and total abundances^a for HV (NGC 6822), NGC 5408, Tol 1924–416, NGC 3125, and Mkn 1271

	HV (NGC 6822)		NGC 5408		Tol 1924–416		NGC 3125		Mkn 1271	
	$t^2 = 0.000$	$t^2 = 0.056$ ± 0.020	$t^2 = 0.000$	$t^2 = 0.147$ ± 0.017	$t^2 = 0.000$	$t^2 = 0.062$	$t^2 = 0.000$	$t^2 = 0.071$ ± 0.020	$t^2 = 0.000$	$t^2 = 0.142$ ± 0.031
Ionic abundances from collisionally excited lines										
N ⁺	5.81 ± 0.05	5.92 ± 0.06	5.48 ± 0.06	5.77 ± 0.05	5.77 ± 0.05	5.88:	6.26 ± 0.05	6.43 ± 0.06	6.08 ± 0.07	6.58 ± 0.16
O ⁺	7.22 ± 0.03	7.34 ± 0.05	6.96 ± 0.04	7.26 ± 0.05	7.17 ± 0.03	7.29:	7.46 ± 0.06	7.64 ± 0.07	7.57 ± 0.04	8.12 ± 0.20
O ²⁺	8.07 ± 0.06	8.31 ± 0.05	7.73 ± 0.03	8.16 ± 0.04	7.92 ± 0.04	8.12:	8.23 ± 0.07	8.65 ± 0.08	7.96 ± 0.06	8.58 ± 0.15
Ne ²⁺	7.38 ± 0.08	7.64 ± 0.12	7.10 ± 0.04	7.55 ± 0.07	7.26 ± 0.06	7.48:	7.60 ± 0.09	8.06 ± 0.17	7.35 ± 0.08	8.02 ± 0.25
S ⁺	5.32 ± 0.04	5.43 ± 0.05	5.23 ± 0.04	5.52 ± 0.05	5.40 ± 0.04	5.51:	5.64 ± 0.04	5.81 ± 0.06	5.74 ± 0.06	6.24 ± 0.16
S ²⁺	6.43 ± 0.09	6.69 ± 0.12	5.94 ± 0.04	6.40 ± 0.07	6.05 ± 0.06	6.27:	6.46 ± 0.10	6.93 ± 0.18	6.10 ± 0.09	6.78 ± 0.26
Cl ²⁺	4.51 ± 0.07	4.74 ± 0.11	4.02 ± 0.05	4.44 ± 0.07	4.25 ± 0.09	4.44:	4.58 ± 0.11	4.98 ± 0.15	4.21 ± 0.09	4.81 ± 0.21
Cl ³⁺	3.89 ± 0.25	4.19 ± 0.19	3.88 ± 0.09	4.25 ± 0.07	3.76 ± 0.11	3.93:	–	–	–	–
Ar ²⁺	5.90 ± 0.06	6.10 ± 0.09	5.45 ± 0.03	5.82 ± 0.07	5.53 ± 0.04	5.70:	5.82 ± 0.11	6.18 ± 0.14	5.60 ± 0.06	6.14 ± 0.19
Ar ³⁺	4.75 ± 0.08	4.99 ± 0.11	5.04 ± 0.03	5.48 ± 0.07	5.02 ± 0.06	5.22:	4.96 ± 0.10	5.39 ± 0.16	5.07 ± 0.08	5.70 ± 0.22
Fe ²⁺	4.91 ± 0.19	5.16 ± 0.15	4.76 ± 0.08	5.20 ± 0.08	5.33 ± 0.09	5.54:	5.59 ± 0.24	6.02 ± 0.18	5.08 ± 0.12	5.71 ± 0.23
Ionic abundances from recombination lines										
He ⁺	10.90 ± 0.01		10.90 ± 0.01		10.86 ± 0.01		10.89 ± 0.02		10.85 ± 0.02	
He ²⁺	–		8.98 ± 0.02		8.87 ± 0.03		–		8.46 ± 0.08	
C ²⁺	7.66 ± 0.09		7.32 ± 0.14		–		8.03:		7.84:	
O ²⁺	8.31 ± 0.04		8.16 ± 0.04		8.12:		8.65 ± 0.08		8.58 ± 0.15	
Total abundances										
He	10.91 ± 0.01		10.91 ± 0.01		10.86 ± 0.01		10.90 ± 0.02		10.85 ± 0.02	
C	7.83 ± 0.10		7.59 ± 0.15		–		8.18:		8.27:	
N	6.72 ± 0.06	6.94 ± 0.09	6.32 ± 0.08	6.72 ± 0.08	6.59 ± 0.06	6.77:	7.10 ± 0.08	7.48 ± 0.12	6.62 ± 0.08	7.17 ± 0.30
O	8.13 ± 0.02	8.35 ± 0.05	7.80 ± 0.02	8.21 ± 0.04	7.99 ± 0.02	8.18:	8.30 ± 0.02	8.69 ± 0.08	8.11 ± 0.02	8.71 ± 0.13
Ne	7.44 ± 0.10	7.68 ± 0.14	7.17 ± 0.05	7.61 ± 0.09	7.33 ± 0.08	7.54:	7.67 ± 0.12	8.10 ± 0.21	7.50 ± 0.10	8.15 ± 0.34
S	6.62 ± 0.08	6.90 ± 0.12	6.16 ± 0.03	6.59 ± 0.07	6.27 ± 0.05	6.47:	6.66 ± 0.09	7.18 ± 0.17	6.32 ± 0.07	6.92 ± 0.22
Ar	5.94 ± 0.06	6.14 ± 0.09	5.60 ± 0.02	5.99 ± 0.05	5.66 ± 0.03	5.83:	5.89 ± 0.10	6.25 ± 0.12	5.75 ± 0.05	6.30 ± 0.16
Fe	5.70 ± 0.21	6.05 ± 0.17	5.49 ± 0.09	6.03 ± 0.10	6.05 ± 0.10	6.31:	6.32 ± 0.27	6.94 ± 0.22	5.54 ± 0.14	6.22 ± 0.36

^a In units of $12 + \log(X^{+n}/H^+)$.

4.2 Ionic abundances and abundance discrepancy

Ionic abundances of N^+ , O^+ , O^{2+} , Ne^{2+} , S^+ , S^{2+} , Cl^{2+} , Cl^{3+} , Ar^{2+} , Ar^{3+} , and Fe^{2+} have been derived from CELs under the two-zone scheme and not considering temperature fluctuations in the gas ($t^2 = 0$, see below) using the PYNEB package (version 0.9.3) and the atomic dataset indicated in Table 5. In PYNEB, an atom is represented as an n -level system and computes the line emissivities as a function of the physical conditions, n_e and T_e . The final results are presented in Tables 7 and 8. We have assumed $T(\text{low})$ to calculate the abundances of low ionization potential ions: N^+ , O^+ , and S^+ ; and $T(\text{high})$ for the rest. We have adopted a mean representative n_e for all the ions in each object. All of them are in the low-density regime, therefore the results do not depend on the precision of the adopted n_e . A number of [Fe II] lines have been detected in the spectra of some of our sample objects. These lines are severely affected by continuum fluorescence effects (see Rodríguez 1999; Verner et al. 2000) and are not suitable for abundance determinations. Unfortunately, the brightest and less sensitive to fluorescence [Fe II] line, [Fe II] 8616 Å is in one of our observational gaps. In Figure 3 we compare the O^{2+} abundances we determined from CELs and those calculated by Guseva et al. (2011) from the same dataset for the same objects. In the figure we have also included values from VLT data for the H II galaxy NGC 5253, which analysis was published by López-Sánchez et al. (2007). These authors used a similar methodology as in this paper so their data can be considered as part of this work. Although the areas extracted by Guseva et al. (2011) and us for their spectroscopical analysis may be different in some objects – perhaps in the case of NGC 5408 – there is a general good agreement because most of the points lie very close of the 1:1 relation line. This is expected for independent similar calculations based on the same data. It is remarkable that since the error bars of all our abundance determinations –except NGC 5408– intersect the 1:1 relation line, none of the error bars quoted by Guseva et al. (2011) intersect it at all. This fact suggests that the uncertainties calculated by those authors might be underestimated.

We have measured many He I emission lines in the spectra of all objects. To derive the He^+ abundance, we used the effective recombination coefficients of Storey & Hummer (1995) for H I and those computed by Porter et al. (2012, 2013) for He I, whose calculations include corrections for collisional excitation and self-absorption effects. The finally adopted He^+/H^+ ratio for each object has been derived from a maximum likelihood method (MLM, Peimbert et al. 2000, 2002). With this method we obtain the best pair of values of mean He^+/H^+ ratio and temperature fluctuations parameter – t^2 , in this case we designate it as $t^2(\text{He I})$ – that minimize the χ^2 of the MLM. For that procedure, we used a number of He I lines ranging from 5 to 15 depending on the object. Table 9 shows the values of $t^2(\text{He I})$ we obtain for all the objects and those estimated assuming that the abundance discrepancy factor for O^{2+} – $\text{ADF}(\text{O}^{2+})$, see definition in Equation 1 – is produced by temperature fluctuations in the ionised gas (see below). As we can see the t^2 values we obtain from both methods are in general consistent except in the case of NGC 5408. It is clear that since the t^2 parameter determined from the $\text{ADF}(\text{O}^{2+})$ concerns

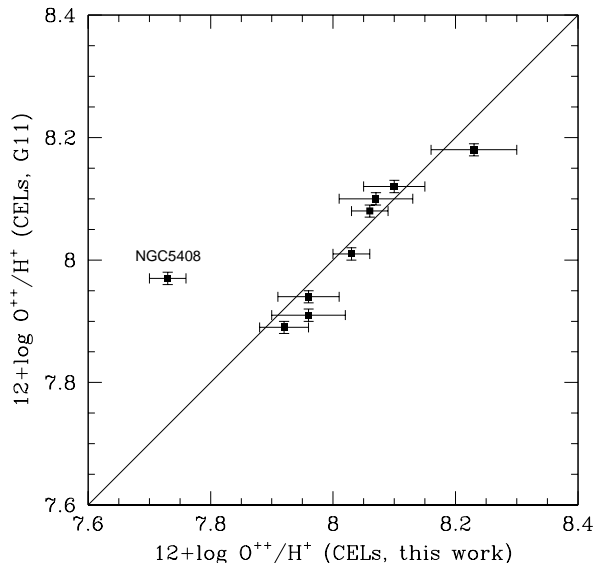


Figure 3. Comparison of the O^{2+} abundances we determine from collisionally excited lines (CELs) and those determined by Guseva et al. (2011) from the same dataset for the same objects. The continuous line is the 1:1 relation. Note that our quoted errors are consistent –as expected– with the 1:1 relation. In contrast, the errors quoted by Guseva et al. (2011) are much smaller and not consistent with that relation. The large discrepancy for NGC 5408 is due to the different areas of the object extracted in both studies. We include values from VLT spectra of the H II galaxy NGC 5253 published by López-Sánchez et al. (2007) as part of this work (average values of their zones A and B).

to the zone of the nebula where O^{2+} is present and $t^2(\text{He I})$ is representative for the whole ionized gas. However, in the sample objects, the O^{2+}/O^+ ratio is between 2.5 and 7.0, indicating that both zones have a large common volume. The only object with previous determination of t^2 is HV in NGC 6822. Peimbert & Peimbert (2005) obtain a value of 0.076 ± 0.018 for it based on the $\text{ADF}(\text{O}^{2+})$, consistent with our t^2 determinations within the uncertainties. The values of the t^2 we calculate in the objects investigated in this paper are among the highest we have found in H II regions. In the compilations presented by López-Sánchez et al. (2007) and Esteban et al. (2009), we can see that only NGC 2363 – a giant H II region in the dwarf H II galaxy NGC 2366 – for which Esteban et al. (2009) determined a t^2 of about 0.120, show a similar high value. Therefore, giant H II regions in dwarf star-forming galaxies present the highest t^2 values. This may perhaps be related to their complex structure and dynamics due to the action of stellar winds and supernova remnants as it was firstly advocated by Peimbert et al. (1991) or even the hardening of the energy distribution of ionizing photons as the central clusters evolve (Perez 1997). Although the simple Peimbert’s formalism (Peimbert 1967) may be not completely adequate for such large temperature fluctuations, we consider it is still useful for parameterizing the problem until their existence and nature are definitely proven.

We have obtained good signal-to-noise ratio measure-

Table 8. Ionic and total abundances^a for POX 4, SDSS J1253–0312, Tol 1457–262, and He 2–10

	POX 4		SDSS J1253–0312	Tol 1457–262	He 2–10
	$t^2 = 0.000$	$t^2 = 0.060$:	$t^2 = 0.000$	$t^2 = 0.000$	$t^2 = 0.000$
Ionic abundances from collisionally excited lines					
N ⁺	5.77 ± 0.06	5.91:	5.96 ± 0.07	6.15 ± 0.05	7.53 ± 0.09
O ⁺	7.23 ± 0.03	7.38:	6.81 ± 0.04	7.58 ± 0.03	8.41 ± 0.10
O ²⁺	8.03 ± 0.03	8.24:	7.96 ± 0.05	8.10 ± 0.05	8.00 ± 0.08
Ne ²⁺	7.35 ± 0.04	7.58:	7.32 ± 0.06	7.46 ± 0.08	7.16 ± 0.14
S ⁺	5.45 ± 0.07	5.59:	5.29 ± 0.09	5.84 ± 0.04	6.30 ± 0.10
S ²⁺	6.17 ± 0.14	6.40:	6.10 ± 0.07	6.35 ± 0.07	6.77 ± 0.08
Cl ²⁺	4.21 ± 0.09	4.41:	4.08 ± 0.12	4.65 ± 0.14	–
Ar ²⁺	5.54 ± 0.05	5.72:	5.57 ± 0.06	5.79 ± 0.05	6.01 ± 0.07
Ar ³⁺	5.17 ± 0.06	5.38:	5.21 ± 0.09	5.14 ± 0.11	–
Fe ²⁺	5.23 ± 0.12	5.45:	5.24 ± 0.09	5.73 ± 0.10	6.21 ± 0.10
Ionic abundances from recombination lines					
He ⁺	10.85 ± 0.02		10.90 ± 0.02	10.89 ± 0.02	10.74 ± 0.02
He ²⁺	9.03 ± 0.03		8.82 ± 0.04	8.70 ± 0.07	–
C ²⁺	8.02:		7.61:	–	–
O ²⁺	8.24:		7.86:	–	–
Total abundances					
He	10.86 ± 0.02		10.90 ± 0.02	10.89 ± 0.02	–
C	8.11:		7.70:	–	–
N	6.63 ± 0.07	6.83:	7.14 ± 0.08	6.78 ± 0.06	7.67 ± 0.14
O	8.09 ± 0.02	8.30:	7.99 ± 0.02	8.21 ± 0.02	8.55 ± 0.02
Ne	7.41 ± 0.05	7.63:	7.35 ± 0.08	7.57 ± 0.10	7.71 ± 0.16
S	6.39 ± 0.12	6.67:	6.41 ± 0.06	6.55 ± 0.05	6.90 ± 0.08
Ar	5.70 ± 0.04	5.89:	5.73 ± 0.05	5.90 ± 0.05	6.31 ± 0.22
Fe	5.98 ± 0.13	6.25:	6.28 ± 0.11	6.28 ± 0.12	6.34 ± 0.16

^a In units of $12+\log(X^{+n}/H^+)$.

ments of the intensity of C II 4267 Å line in HV (NGC 6822) and NGC 5408. In the cases of Mkn 1271, NGC 3125, POX4, and SDSS J1253–0312 the error of the intensity of that line is of the order or larger than 40%, and does not permit to derive a precise value of the ionic abundance. C II 4267 Å has not been detected in Tol 1457–262 and He 2–10. However, Guseva et al. (2011) report good measurements of the intensity of C II 4267 Å in all the sample objects except in SDSS J1253–0312 – its error is somewhat larger than 40% – and He 2–10, for which they derive an upper limit. This disagreement has not a clear explanation for us considering that we are analysing the same spectral dataset and that – as it has been said before – we optimized the extracted areas in order to isolate the brightest knots for each object. These knots coincide with the position of the ionizing sources and therefore where the bulk of C²⁺ emission should be concentrated.

The lower panel of Figure 4 compares our line intensity ratios of C II 4267 Å with respect to Hβ with those obtained by Guseva et al. (2011). As we can see, some values do not agree, but there is not a systematical difference between both sets of determinations. C II 4267 Å is a pure RLs and permits to derive the C²⁺/H⁺ ratio. We have used $T(\text{high})$ and the effective recombination coefficients of Davey et al. (2000) to obtain the C²⁺ abundance of the objects, which is included in Tables 7 and 8. The upper panel of Figure 4 shows that the C²⁺/H⁺ ratios we obtain for the sample ob-

Table 9. Values of t^2 .

Object	$t^2(\text{ADF})^a$	$t^2(\text{He I})^b$
He 2–10	–	0.020 ^{+0.054} _{–0.020}
Mkn 1271	0.142±0.031	0.167±0.026
NGC 3125	0.071±0.020	0.081±0.036
NGC 5408	0.147±0.017	0.063±0.034
HV (NGC 6822)	0.056±0.020	0.080±0.030
POX 4	0.060:	0.068±0.048
SDSS J1253–0312	–	0.052 ^{+0.064} _{–0.052}
Tol 1457–262	–	0.049 ^{+0.052} _{–0.049}
Tol 1924–416	0.062:	0.116±0.033

^a t^2 estimated from the ADF(O²⁺).

^b t^2 estimated from the MLM used for determining the He⁺/H⁺ ratio.

jects – including data for NGC 5253 (López-Sánchez et al. 2007) – are systematically larger than those determined by Guseva et al. (2011) except in the case of NGC 5408. The fact that this systematic difference is not seen in the lower panel and that we are using the same set of effective recombination coefficients suggests that the source of the disagreement should come from the different – or inappropriate – calculation procedure used to derive the abundances.

We obtain good measurements of RLs of O II in the cases of HV (NGC 6822), Mkn 1271, NGC 3125, and NGC 5408

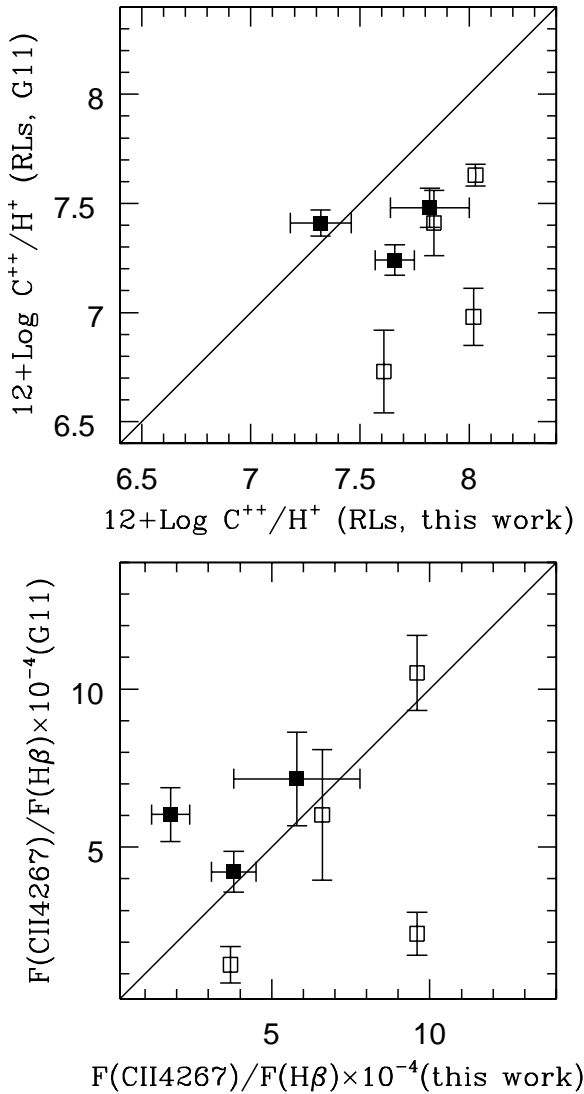


Figure 4. Upper panel: comparison of the C^{2+} abundances we determine from the $C\text{ II } 4267\text{ \AA}$ recombination line (RL) and those calculated by Guseva et al. (2011) from the same dataset for the same objects. The solid lines represents the 1:1 relation. The filled squares represent objects for which we have good determinations of the intensity of the $C\text{ II } 4267\text{ \AA}$ line, open squares are objects for which we report errors larger than 40% in the intensity of that line. We include values from VLT spectra of the H II galaxy NGC 5253 published by López-Sánchez et al. (2007) as part of the sample of this work. Lower panel: the same but comparing derreddened line intensity ratios of $C\text{ II } 4267\text{ \AA}$ with respect to $H\beta$.

and with errors of the order or larger than 40% in POX 4, Tol 1924–416, and SDSS J1253–0312. Guseva et al. (2011) obtain good measurements – errors in the line intensities always better than 35% – in He 2–10, HV (NGC 6822), Mkn 1271, NGC 3125, NGC 5408, and POX 4. It is striking that Guseva et al. (2011) give an error of 15% for the blend of O II lines at 4649.13 and 4650.84 Å in He 2–10 since we do not detect such feature in our spectrum. In Figure 5 we com-

pare the line intensity ratios of the blend of O II 4649.13 and 4650.84 Å lines with respect to $H\beta$ obtained by Guseva et al. (2011) and in this work, finding no systematic differences. Following our usual methodology to minimize uncertainties, we have derived the O^{2+} abundance from the estimated total intensity of the RLs of multiplet 1 of O II (see Equation 7 of Esteban et al. 2009). The lines of multiplet 1 of O II are not in LTE for densities $n_e < 10^4\text{ cm}^{-3}$ (Ruiz et al. 2003), and this is the case for all our sample objects. Therefore, we have used the prescriptions given by Peimbert et al. (2005) to calculate the appropriate corrections for the relative strengths between the individual lines of multiplet 1. The O^{2+} abundances from RLs have been calculated using T (high) and the effective recombination coefficients of Storey (1994) assuming LS coupling and they are included in Tables 7 and 8. In contrast to that we found in the comparison of C^{2+} abundances, we do not find systematic differences between the O^{2+}/H^+ ratios determined by us and the values given by Guseva et al. (2011). In this case, there seems to be no discrepancies between the methods for determining the O^{2+} abundance used by both research groups.

The spectra of some of the sample objects also show permitted lines of other heavy-element ions as N I, N II, N III, O I and/or Si II, but they are produced by fluorescence and can not be used to derive reliable abundance values (see Esteban et al. 1998, 2004).

For HV (NGC 6822), Mkn 1271, NGC 3125, and NGC 5408, the high signal-to-noise ratio of the spectra has permitted to calculate O^{2+} abundances from both kinds of lines RLs and CELs. In the cases of POX 4, Tol 1924–416, and SDSS J1253–0312 the abundance determinations based on RLs are rather uncertain due to the faintness of the lines. It is important to remark that – except for SDSS J1253–0312 – the O^{2+} abundance determined from RLs is always larger than that obtained from CELs, with differences ranging from 0.20 and 0.62 dex. This difference is the so-called abundance discrepancy O^{2+} , $ADF(O^{2+})$, which is defined as:

$$ADF(O^{2+}) = \log(O^{2+}/H^+)_{RLs} - \log(O^{2+}/H^+)_{CELs}. \quad (1)$$

Positive values of the $ADF(O^{2+})$ have been found in all H II regions where O II RLs lines have been measured with enough signal-to-noise ratio (e.g. García-Rojas & Esteban 2007; Esteban et al. 2009). The mean value of the $ADF(O^{2+})$ found for Galactic and extragalactic H II regions is 0.26 ± 0.09 (Esteban et al. 2009). The mean of the four objects with the best determinations of the $ADF(O^{2+})$ in the present work (HV, Mkn 1271, NGC 3125 and NGC 5408) is 0.43 ± 0.16 , higher than in the rest of the H II regions reported in the literature. There seems to be no correlation between the $ADF(O^{2+})$ and properties as metallicity, ionization degree or mean electron temperature of the ionized gas.

If – as an hypothesis – and as in other previous spectroscopical studies of our group, we assume the validity of the temperature fluctuations paradigm and that this phenomenon produces the abundance discrepancy (see García-Rojas & Esteban 2007), we can estimate the t^2 parameter that produces the agreement between the abundance of O^{2+} determined from CELs and RLs, $t^2(ADF)$. Table 9 compiles the values of $t^2(ADF)$ obtained for the objects. Tables 7 and 8 list the ionic abundances determined for

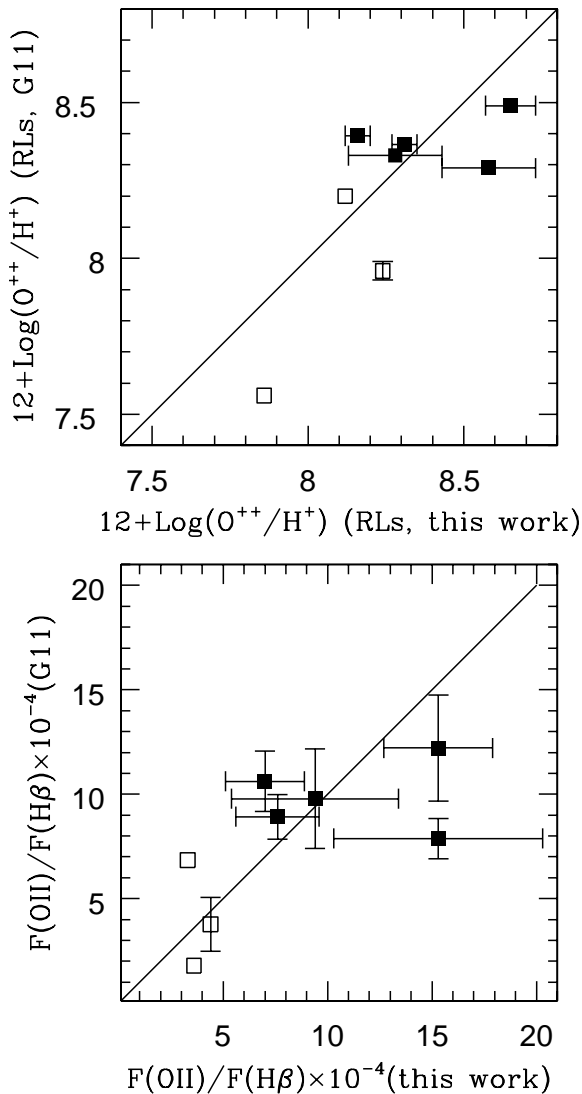


Figure 5. Comparison of the dereddened intensity ratios of the O II 4649.13 + 4650.84 Å lines with respect to H β and those obtained by Guseva et al. (2011) from the same dataset for the same objects. The solid line represents the 1:1 relation. The filled squares represent objects for which we have good determinations of the intensity of the O II lines, open squares are objects for which we report errors larger than 40%. We include values from VLT spectra of the H II galaxy NGC 5253 published by López-Sánchez et al. (2007) as part of the sample of this work.

$t^2 = 0$ – the standard procedure when not considering temperature fluctuations – and assuming the estimated t^2 (ADF) values and their associated uncertainties. These last calculations have been made following the formalism outlined by Peimbert & Costero (1969) and updated by Peimbert et al. (2002).

4.3 Gas-phase total abundances

We have adopted a set of ionization correction factors (ICFs) to correct for the unseen ionization stages and derive the total gas-phase abundances of the different elements, except in the case of O for which we have measured emission lines of all the main expected ionic species. The adopted total abundances for $t^2 = 0$ and $t^2 > 0$ are presented in Tables 7 and 8. For those objects without detection of He II lines – HV (NGC 6822), NGC 3125, and He 2–10 – the total helium abundance has been corrected for the presence of neutral helium using the ICFs obtained from the photoionization models of Stasińska (1990) that reproduce the O abundance, O^{2+}/O^+ ratio, $T_e([O III])$ and $T_e([O II])$ determined for each object. In the case of He 2–10, we have not been able to obtain a precise value of the total He abundance due to its low ionization degree that implies a large contribution of neutral He and a very uncertain ICF. The total He abundance of the rest of the sample objects have been calculated adding the He^+/H^+ and He^{2+}/H^+ ratios, the contribution of this last ion is almost negligible in all the objects. The weakness of the He II 4686 Å lines implies that the amount of O^{3+} inside the nebulae is irrelevant, validating our assumption of no considering an ICF for O.

For C, we have adopted an ICF derived from photoionization models of Garnett et al. (1999). This correction seems to be fairly appropriate considering the high ionization degree of the nebulae where the C II 4267 Å line has been detected. In order to derive the total abundance of nitrogen we have used the usual ICF based on the similarity of the ionization potential of N^+ and O^+ (Peimbert & Costero 1969). The only measurable CELs of Ne in the optical range are those of Ne^{2+} but the fraction of Ne^+ may be important in the nebulae. We have adopted the usual expression of Peimbert & Costero (1969) that assumes that the ionization structure of Ne is similar to that of O. We have measured CELs of two ionization stages of S: S^+ and S^{2+} , and used the ICF proposed by Stasińska (1978) to take into account the presence of some S^{3+} . For argon, we have determinations of Ar^{2+} and Ar^{3+} but some contribution of Ar^+ is also expected. We have adopted the ICF recommended by Izotov et al. (1994) for this element. Finally, we have used an ICF scheme based on photoionization models of Rodríguez & Rubin (2005) to obtain the total Fe/H ratio from the Fe^{2+}/H^+ ratio. The variations due to the dependence of the adopted ICFs on the t^2 considered are also included in the total abundances given in Tables 7 and 8. We have made the exercise of estimating the total abundances of several elements in the case of using other ICFs as the scheme proposed by Izotov et al. (2006) based on photoionization model grids. We find that the differences are not very significant except in rather few cases. Our determinations of the N and Ne abundances are in average about 0.04 dex higher than those calculated making use of the formulae of Izotov et al. (2006). In the case of S, the average difference is higher, being our S/H ratios 0.09 dex lower than those obtained with the alternative ICF scheme. The differences are much larger in the cases of SDSS J1253–0312 and He 2–10 – precisely our objects with the highest and lowest ionization degrees, respectively – for which our S abundances are 0.22 and 0.32 dex – respectively – lower than those estimated using the formulation of Izotov et al. (2006). Finally,

our Ar abundances are only about 0.02 dex higher except in the case of He 2–10, where the difference is about 0.22 dex.

5 DISCUSSION

5.1 The C/O vs. O/H relation

Determining the C/O ratios in extragalactic H II regions and H II galaxies permits to explore the chemical evolution of C in low-metallicity objects. Figure 6 plots the C/O vs. O/H ratios for the complete sample of H II regions where C and O abundances have been determined from RLs: HV (NGC 6822) and NGC 5408 from this work, Galactic H II regions (García-Rojas & Esteban 2007; Esteban et al. 2013), H II regions in external spiral and irregular galaxies (Peimbert 2003; Esteban et al. 2009) and the blue compact dwarf galaxy NGC 5253 (López-Sánchez et al. 2007). The peculiar position of NGC 2363 is indicated in Figure 6 because it will be discussed later. The figure shows the well-known C/O vs. O/H correlation found in previous works by, for example, Garnett et al. (1995, 1999) from observations of CELs or Esteban et al. (2002, 2009) from observations of RLs.

Figure 6 includes the time evolution of the abundances predicted by the chemical evolution models of the Milky Way disc presented by Esteban et al. (2013). These models reproduce the observed radial C, O, and C/O gradients determined by Esteban et al. (2005, 2013). The solid line represents the time evolution of abundances at $R_G = 8$ kpc since the epoch of the formation of the Galactic disc, from $t_G \sim 1$ Gy up to the present. The dotted line connecting with the solid line indicates the chemical evolution at that part of the Galaxy for $t_G < 1$ Gy, corresponding to the epoch of the formation of the Galactic halo. The long-dashed line connected with another dotted line represents the chemical evolution at $R_G = 4$ kpc during the halo and disc formation. The short-dashed line represents the same for $R_G = 14$ kpc.

The main assumptions of the chemical evolution model by Esteban et al. (2013) are described in the following:

i) The Milky Way disc was formed in an inside-out scenario from primordial infall with time scales $\tau = r(\text{kpc}) - 2$ Gyr.

ii) The star formation rate (SFR) is a spatial and temporal function of the form:

$$\text{SFR}(r, t) = \nu(r) \times M_{\text{bar}}^{1.4}(r, t) \times M_{\text{gas}}^{0.4}(r, t); \quad (2)$$

where M_{gas} and M_{bar} are the surface mass density of gas and baryonic masses; ν is r -dependent to reproduce the behaviour of the O/H gradient in the Galactic disk.

iii) The initial mass function is that by Kroupa et al. (1993) in the $0.08 - 80 M_{\odot}$ range.

iv) We consider an array of metal dependent yields:

- a) for LIM stars ($0.8 \leq m/M_{\odot} \leq 8$), we use the yields by Marigo et al. (1996, 1998) and Portinari et al. (1998);
- b) for massive stars ($8 \leq m/M_{\odot} \leq 80$) we considered the yields including stellar rotation by Hirschi (2007) and Meynet & Maeder (2002) for $Z \leq 0.004$; and the intermediate wind yields, obtained as an average of the yields by Maeder (1992, high mass-loss rate) and Hirschi et al. (2005, low mass-loss rate) for $Z = 0.02$.

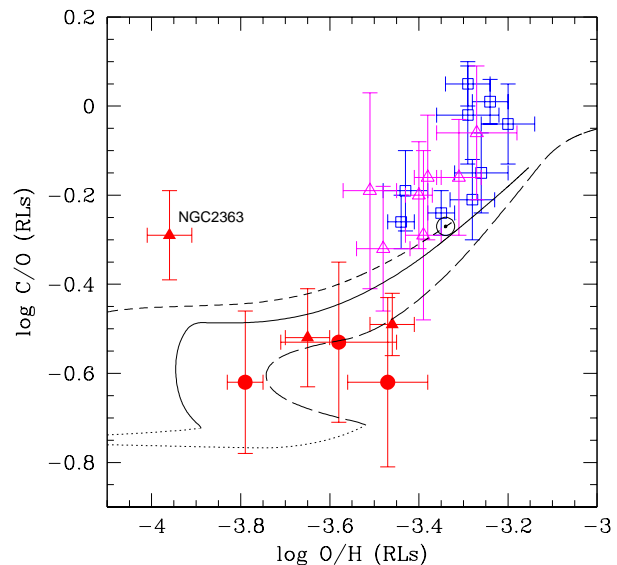


Figure 6. C/O vs. O/H ratios of Galactic and extragalactic H II regions determined from recombination lines. open (blue) squares represent data for Galactic H II regions (García-Rojas & Esteban 2007; Esteban et al. 2013); open (magenta) triangles correspond to H II regions in the inner discs of external spiral galaxies (Esteban et al. 2009); full (red) triangles indicate abundance ratios for H II regions in irregular galaxies (this work; Peimbert 2003; Esteban et al. 2009) and full (red) circles correspond to dwarf star-forming galaxies (classified as H II galaxies or blue compact dwarves: this work; López-Sánchez et al. 2007). The solar symbol represents the abundances of the Sun (Asplund et al. 2009). The lines show the predictions of chemical evolution models presented by Esteban et al. (2013) for the Milky Way. The solid line represents the time evolution of abundances since the formation of the Galactic disc ($t_G > 1$ Gy) for $R_G = 8$ kpc, the long- and short-dashed lines represent the same but for $R_G = 4$ and 14 kpc, respectively. Dotted lines represent the evolution for the same radii but for $t_G < 1$ Gy, during the formation of the Galactic halo. We recommend to add ~ 0.1 dex to the $\log(\text{O}/\text{H})$ values of H II regions to correct for dust depletion. No correction is needed for their C/O ratios (see §5.1 for details).

Our model is in agreement with competing classical chemical evolution models (without dynamical considerations) in broad outlines, but it disagrees on some details. For example, our model explains the rise in C/O for metal-poorer thick disk stars due to LIM stars of low Z and the high C/O for metal-richest thin disk stars due to massive stars of high Z , but Cescutti et al. (2009) explain the C/O ratios in disk stars due to massive stars alone. Most chemical evolution models need to improve their agreement with the gaseous and stellar N abundances (Carigi et al. 2005; Romano et al. 2010; Kobayashi et al. 2011). The disagreement is due mainly to the uncertainties in the N yields (Karakas & Lattanzio 2007) due to its complex nucleosynthesis. Moreover, our model, as classical ones, cannot reproduce the alpha-element enhancement shown by the thick disk stars compared to thin disk ones because it does not consider dynamical aspects (see Minchev et al. 2013, and references therein).

It must be remarked that the C and O abundances of the H II regions presented in Figure 6 have not been corrected for the fraction of atoms embedded in dust and this should be taken into account when comparing with stellar or solar abundances or the results from chemical evolution models. According to Mesa-Delgado et al. (2009) the fraction of O embedded in dust grains in the Orion Nebula is about 0.12 dex. Peimbert & Peimbert (2010) have estimated that the depletion of O increases with increasing O/H. They propose that O depletion ranges from about 0.08 dex, for the metal poorest H II regions, to about 0.12 dex – the value estimated for the Orion Nebula – for metal-rich H II regions. C is also expected to be depleted in dust, mainly in polycyclic aromatic hydrocarbons and graphite, though the study of its depletion is certainly problematic (see Mathis 1996). The paucity of observational information makes that the C abundance in the gas and dust phases of the diffuse interstellar medium is something very poorly understood (see Sofia et al. 2011, and references therein). The different estimations of the amount of C locked up in dust grains in the local interstellar medium show a rather large variation depending on the abundance determination methods applied (see Jenkins 2014). Assuming the quantities compiled by Jenkins (2014) we find that the gas+dust C/H ratios in the Orion Nebula would be between 0.09 to 0.26 dex larger than the ionized gas phase values determined by Esteban et al. (2004). However, some degree of destruction of C-bearing dust particles is likely to be acting in ionized nebulae and the assumption of depletion factors of the neutral diffuse interstellar medium may not be appropriate for an ionized nebula. On the other hand, assuming the protosolar C abundance given by Asplund et al. (2009) – corrected for the amount of this element produced by the chemical evolution of the Galaxy that those authors propose – we find a dust depletion of the order of 0.10 dex for the Orion Nebula, in agreement with the estimate by Esteban et al. (1998). Taking into account (a) the uncertain degree of depletion of C in local objects, (b) the indications that this seems to be not very different to that of O and (c) the complete lack of estimations for lower metallicities, we consider reasonable to assume no correction for the C/O ratio. As a conclusion, we recommend to increase nebular O/H values by about 0.08-0.12 dex but not the C/O ratio when comparing those ratios with the predictions of chemical evolution models or solar or stellar abundances.

Following Figure 6, it is evident that H II regions in irregular and H II galaxies – except NGC 2363 – show systematically lower values of C/O and somewhat lower O/H than H II regions belonging to the inner discs of spiral galaxies. Therefore, both kinds of objects occupy different loci in the diagram, indicating different chemical evolution histories. In fact, star formation in dwarf galaxies are dominated by bursts and the particular star formation history of each object may be very different (e.g. López-Sánchez & Esteban 2010; Karthick et al. 2014). In the diagram – and considering the dust correction commented above – we can see that the Galactic disc models match quite well the distribution of the points corresponding to spiral galaxies. Chemical evolution models for local dwarf spheroidal galaxies (dSphs), as those by Carigi et al. (2002), are able to reproduce the range of C/O and O/H ratios observed in H II regions belonging to dwarf irregular galaxies. This agreement is due to the sim-

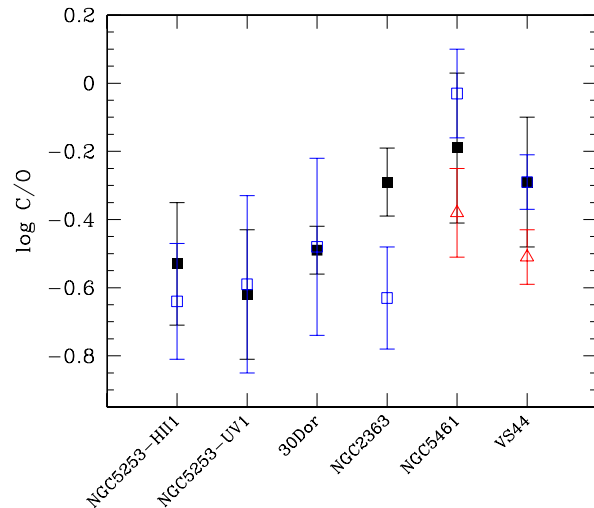


Figure 7. C/O for extragalactic H II regions determined from recombination lines (RLs, black filled squares) as well as from collisionally excited lines (CELs) in the UV (open colored symbols) for extragalactic H II regions where these two determinations are available in the literature. In the case of NGC 5461 and VS 44, the blue open squares and the red open triangles represent values obtained assuming two different reddening laws in the UV. See §5.1 for references.

ilarity between the early bursts of star formation in dSphs and the recent bursts of star formation in dwarf irregulars (see Skillman et al. 2014, their figure 9).

In ionized nebulae, the C/O ratio can also be determined from the intensity of CELs of C^{2+} and O^{2+} in the UV. Based on that kind of lines, Garnett et al. (1995, 1997), Kobulnicky et al. (1997), Kobulnicky & Skillman (1998), and Izotov & Thuan (1999) determined the C/O ratios for a number of metal-poor galaxies. The same was done by Garnett et al. (1999) for a sample of H II regions in the inner discs of spiral galaxies. Figure 7 compares the C/O ratios in objects for which we have determinations based on both kinds of lines, CELs and RLs. The data based on RLs are from López-Sánchez et al. (2007, NGC 5253), Peimbert (2003, 30 Dor) and Esteban et al. (2009, NGC 2363, NGC 5461, and VS 44). The data based on CELs are from: Kobulnicky et al. (1997, NGC 5253), Garnett et al. (1995, 30 Dor, and NGC 2363) and Garnett et al. (1999, NGC 5461, and VS 44). In the cases of NGC 5461 and VS 44, Garnett et al. (1999) give two values of the C/O ratio depending on two different reddening laws they assume in the UV. Figure 7 shows that C/O ratios calculated with CELs and RLs are consistent within the uncertainties except in the case of NGC 2363. The C/O ratio obtained by Esteban et al. (2009) from RLs for this object is substantially higher than that obtained by Garnett et al. (1995) from CELs perhaps because we observe a different zone of the object.

Assuming that $C/O(RLs) \sim C/O(CELs)$ as Figure 7 suggests, we have constructed Figure 8 including the same objects as in Figure 6 but adding data for additional metal-

poor star-forming dwarf galaxies obtained from UV CELs. These last data have been taken from Garnett et al. (1997), Kobulnicky & Skillman (1998), and Izotov & Thuan (1999). The figure permits to explore the C/O vs. O/H relation at lower metallicities. In the sake of consistency and for comparing O abundances determined using the same method, we have represented the O/H ratio determined from CELs and $t^2 = 0$ for all the objects. For our opinion, this is the best solution because objects which C abundance has been determined from UV CELs do not have estimate of their expected $ADF(O^{2+})$ as well as of their corresponding t^2 parameter. Now, in Figure 8, the points that were included in Figure 6 – for which we determined O/H from RLs – are displaced between 0.20 and 0.30 dex towards lower O abundances due to the aforementioned abundance discrepancy problem. The amount of such discrepancy for each object can be noted comparing the O abundance of the points having the same C/O ratios in figures 6 and 8. From Figure 8, it is now more evident that the objects show a clear trend in the sense of increasing the C/O ratio as the O abundance increases. This tendency has been interpreted as the combination of two processes: a) the time delay in the release of C by low- and intermediate-mass (LIM) stars with respect to the O production and b) metallicity-dependent yields of C in massive stars (Garnett et al. 1999; Henry et al. 2000; Carigi 2000; Chiappini et al. 2003). The objects that show some displacement from that trend are indicated in Figure 8: NGC 2363, UM 469, and the two points corresponding to the NE and SW zones of I Zw 18. However, UM 469 presents a large error and its position should be even considered compatible with the general trend considering the uncertainties.

Figure 9 further extends the C/O vs. O/H diagram showing the behaviour of very metal-poor objects: stars of the Galactic halo (Fabbian et al. 2009) and damped Ly α (DLA) systems (Cooke et al. 2011). For the Milky Way, it appears that the amount of C in halo stars is dominated by the contribution from massive stars (e.g. Akerman et al. 2004; Fabbian et al. 2009). Figure 9 shows that the position of metal-poor star-forming dwarf galaxies and halo stars is similar, suggesting the same origin for the production of the bulk of C in those galaxies. Garnett et al. (1995) came to the same conclusion from the comparison of the C/O ratio in dwarf galaxies with the predictions for massive star nucleosynthesis models of Weaver & Woosley (1993). The increase of the C/O toward the lowest metallicities may be the fingerprints of the contribution of Population III stars or the enhanced production of C induced by fast rotation in Population II stars (e.g. Fabbian et al. 2009). It is interesting to note that the two points of I Zw 18 – that were slightly above the extrapolation of the behaviour of other H II regions with higher O/H ratios in Figure 8 – match the general trend of the Galactic halo stars. From the data represented in Figure 9, a minimum of the C/O ratio seems to exist at $\log(O/H) \sim -4.6$. In any case, we must remind that the O abundances for the H II regions represented in Figure 9 have been determined making use of CELs and assuming $t^2 = 0$. Values obtained from RLs would increase the O/H ratios about 0.2 to 0.3 dex in average.

Figure 10 compares the position of the objects represented in Figure 6 with the distribution of abundance ratios in nearby F and G dwarf stars of the Galactic disc (Bensby & Feltzing 2006). In this figure, we have used the

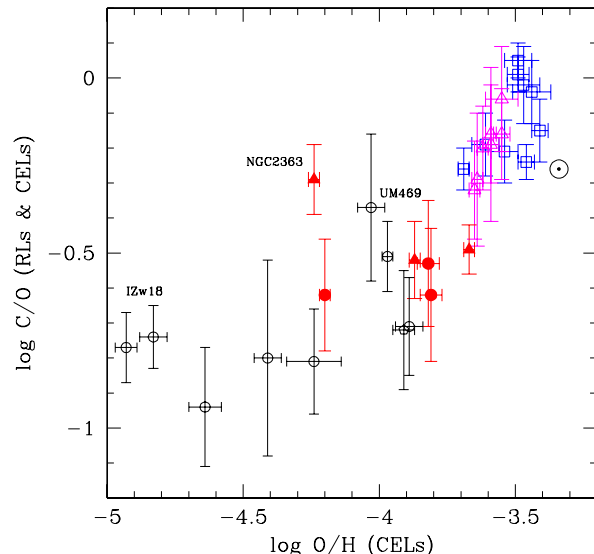


Figure 8. C/O vs. O/H for H II regions in the Milky Way and spiral, irregular and dwarf star-forming galaxies. The O/H ratios are obtained from CELs (considering $t^2 = 0$) and the C/O ratios are determined from either CELs or RLs. Open (blue) squares represent data for Galactic H II regions; open (magenta) triangles correspond to H II regions in the inner discs of external spiral galaxies; full (red) triangles indicate abundance ratios for H II regions in irregular galaxies; full (red) circles correspond to dwarf star-forming galaxies (see references in the caption of Figure 6). Open (black) pentagons represent data for H II regions in irregular galaxies obtained by Garnett et al. (1995); open (black) circles correspond to data for dwarf star-forming galaxies from the works by Garnett et al. (1997), Kobulnicky & Skillman (1998) and Izotov & Thuan (1999). The solar symbol represents the abundances of the Sun (Asplund et al. 2009). We recommend to add ~ 0.1 dex to the $\log(O/H)$ values of H II regions to correct for dust depletion and compare appropriately with solar abundances. No correction is needed for C/O ratios (see §5.1 for details).

O/H ratios determined from RLs instead of CELs. This is because using CELs, the systematic offset between stellar and nebular abundances is between 0.3 and 0.5 dex, much larger than the 0.1 dex expected due to dust depletion. As we discussed in §5.1, the C/O ratios seem to be not significantly affected by neither dust depletion nor the abundance discrepancy problem. Bensby & Feltzing (2006) note that the C/O vs. O/H trend is fairly similar to the well-known Fe/O vs. O/H one, suggesting that LIM stars should be important contributors to the C enrichment at higher metallicities. This was also one of the main results of the chemical evolution models by Carigi et al. (2005). In Figure 10, we can note that the segregation between H II regions belonging to massive and low-mass galaxies is also reflected in the chemical properties of stars of the Galactic thin and thick discs. The locus defined by the stars of the thick disc coincides with that occupied by H II regions in star-forming dwarf galaxies. In contrast, the locus of the thin disc stars is similar to that of H II regions in the inner discs of the more massive spiral galaxies. The origin of the

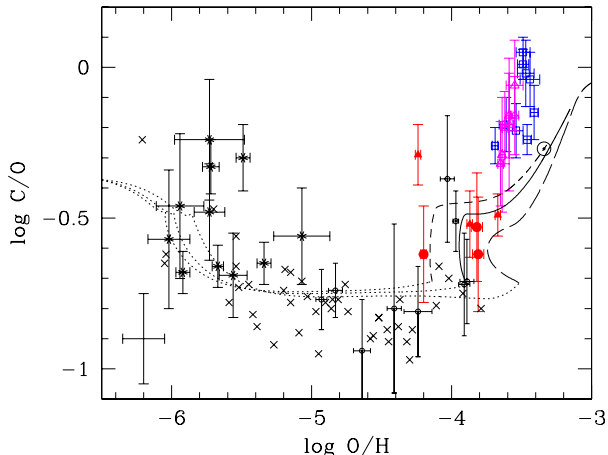


Figure 9. The same as in Figure 8 but also including data for very metal-poor objects: crosses correspond to Galactic halo stars (Fabbian et al. 2009) and asterisks with error bars to DLA systems (Cooke et al. 2011). The typical errorbar for halo stars data is at the bottom left corner of the panel. The lines show the predictions of chemical evolution models presented in Figure 6. We recommend to add ~ 0.1 dex to the $\log(O/H)$ values of H II regions to correct for dust depletion. No correction is needed for their C/O ratios (see §5.1 for details).

Galactic thick disc is still controversial. There are two main competing scenarios: a) it is a result of an ancient merger event between the Milky Way and another dwarf galaxy (e.g. Quinn et al. 1993; Villalobos & Helmi 2009) and b) it is the product of radial mixing of gas and stars from the thin disc (e.g. Schönrich & Binney 2009). In the light of the comparison provided in Figure 10, the C/O *vs.* O/H relation seems to favor the galaxy merger scenario for the origin of the Galactic thick disc, and that the stellar system absorbed by the Milky Way should be a dwarf galaxy.

5.2 The C/O *vs.* N/O relation

Using abundance values determined from UV and optical CELs, Kobulnicky & Skillman (1998) found a possible correlation between C/O and N/O depending on the reddening law they assumed. The exploration of such relation is of much interest to compare the enrichment timescales of C and N. Figure 11 plots the C/O values of the objects included in Figure 8 with respect to their corresponding N/O ratios. This figure also includes data for halo stars of the unmixed subsample of Spite et al. (2005), very metal-poor DLAs (Cooke et al. 2011) and a carbon-enriched very metal-poor DLA reported by Cooke et al. (2012). For H II regions, the N/O ratios have been determined from the intensity of CELs and assuming $t^2 = 0$, because there are no sufficiently bright pure RLs of N in the optical. The N/O ratios of the objects which C/O ratios have been derived from RLs – those included in Figure 6 – have been taken from the

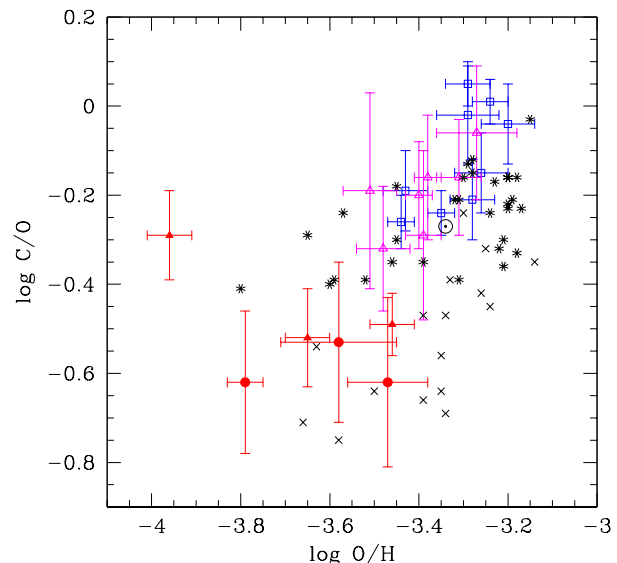


Figure 10. The same as in Figure 6 but also including data for F and G dwarf stars of the Galactic thin and thick discs (asterisks and crosses, respectively) obtained by Bensby & Feltzing (2006). We recommend to add ~ 0.1 dex to the $\log(O/H)$ values of H II regions to correct for dust depletion. No correction is needed for their C/O ratios (see §5.1 for details).

same works as their C/O values (this work; Peimbert 2003; Esteban et al. 2009, 2013; García-Rojas & Esteban 2007; López-Sánchez et al. 2007). For the H II regions which C/O ratio was derived from UV CELs – black open circles and pentagons – their N/O ratios have been taken from the revision of optical emission-line flux ratios of Nava et al. (2006), except in the case of SMC N88A for which we used the value obtained by Testor et al. (2003). Contrary to what happens with C and O, N is expected not being a major constituent of dust, due to its inclusion in the highly stable gas form of N_2 (Gail & Sedlmayr 1986; Jenkins 2014). In the case of Figure 11 we recommend to subtract ~ 0.1 dex to the $\log(N/O)$ values of H II regions to correct for dust depletion in O. Figure 11 shows that H II region data are tightly correlated, with a slope close to 45° . This trend is far more clear and includes more objects than that obtained by Kobulnicky & Skillman (1998) and, moreover, it is independent of the reddening law assumed because it only involves optical emission lines for most of the objects. From the figure, we also see that the chemical evolution models for the Milky Way presented by Esteban et al. (2013) reproduce the position of H II regions in the inner discs of spiral galaxies and the slope of the correlation. However, the models fail to reproduce the position of the halo stars, perhaps because of variations on the initial mass function, the star formation rate or even stochastic effects due to low numbers of massive stars polluting the gas where halo stars born (Carigi & Hernandez 2008).

The apparent coupling between the C and N enrichment we see from H II region data is further suggested in Figure 12, that plots the C/N *vs.* O/H relation for H II regions which C/O ratios derived from RLs as well as halo stars (Spite et al. 2005, unmixed subsample) and very metal-poor

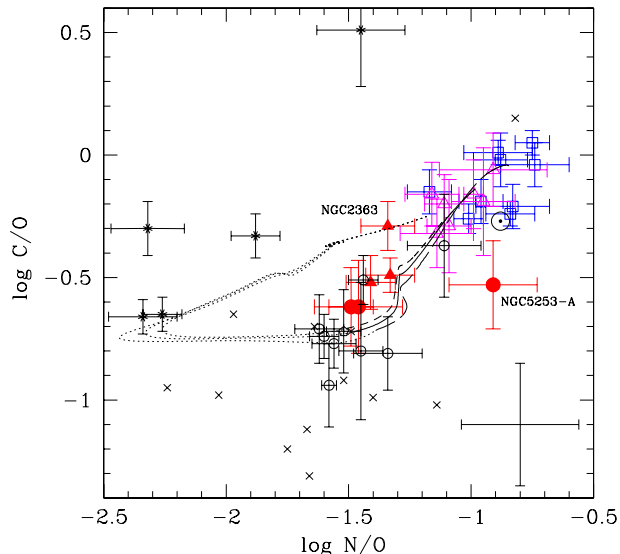


Figure 11. C/O vs. N/O for H II regions in the Milky Way, spiral, irregular and star-forming dwarf galaxies as well as for halo stars (Spite et al. 2005, their unmixed subsample) and very metal poor DLAs (Cooke et al. 2011, 2012). Symbols represent the same as in Figure 8 but now we include data for a carbon enriched metal-poor DLA reported by Cooke et al. (2012) (the object at $C/O = 0.51$). In the case of H II regions, the C/O ratios are obtained from the intensity of either RLs or CELs and the N/O values have been derived from CELs (see text for details and references). The typical errorbar for halo stars data is at the bottom right corner of the panel. The lines show the predictions of chemical evolution models presented in Figure 6. We recommend to subtract ~ 0.1 dex to the $\log(N/O)$ values of H II regions to correct for dust depletion in O (see §5.2 for details).

DLAs (Cooke et al. 2011, 2012). In nebulae, for calculating the C/N ratio we have assumed the N abundances determined from CELs corrected for the presence of temperature fluctuations using the values of t^2 parameter estimated for each object. This is performed to correct for the abundance discrepancy problem assuming that it is related to temperature variations in the nebulae (e.g. García-Rojas & Esteban 2007). On the other hand, the quantities represented in both axes of Figure 12 are expected to be affected by some amount of dust depletion. As we discussed in §5.1, we should add ~ 0.1 dex to both $\log(C/N)$ and $\log(O/H)$ of H II regions in order to correct for dust depletion.

From Figure 12 we can note that, for H II region data, C/N vs. O/H does not show a clear correlation, indicating a rather constant value of C/N in the range of metallicities that those objects occupy. Other authors have explored this relation using abundance data determined from UV and optical CELs, finding either a slight tendency for lower C/N ratios at lower metallicity (Kobulnicky & Skillman 1998) or a lack of correlation (Garnett et al. 1999) as in our case. The chemical evolution models for the Milky Way of Esteban et al. (2013) are able to reproduce the rather constant C/N ratio since the formation of the Galactic disc.

The apparent coupling between the C and N enrichment that we observe from H II region data at high metallicities is

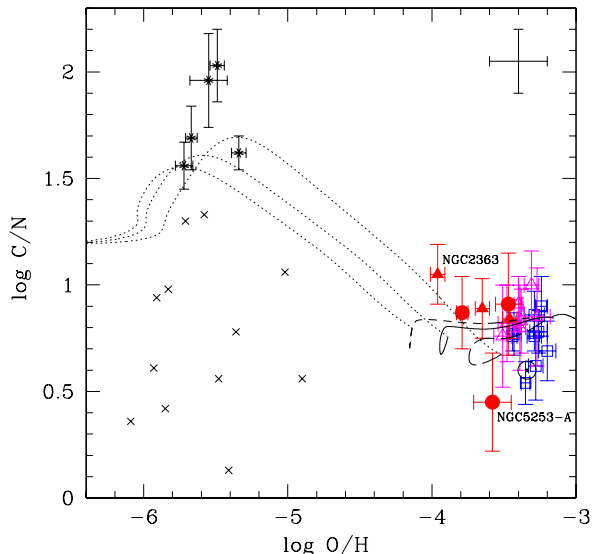


Figure 12. C/N vs. O/H for Galactic and extragalactic H II regions, halo stars and very metal poor DLAs. Symbols represent the same as in Figure 11. In the case of H II regions, C and O abundances are determined from RLs and N ones from CELs and assuming $t^2 > 0$ (see §5.2 for details). The typical errorbar for halo stars data is at the upper right corner of the panel. The lines show the predictions of chemical evolution models presented in Figure 6. We recommend to add ~ 0.1 dex to the values of both $\log(C/N)$ and $\log(O/H)$ of H II regions to correct for dust depletion (see §5.2 for details).

due to the cumulative-temporal contribution of the C and N yields by stars of different masses. The nucleosynthesis processes of both elements are different, but their enrichment timescales result to be rather similar, due to the metallicity-dependent yields and the lifetimes of stars that contribute to the C and N increase. Following Carigi et al. (2005), at high metallicities, $\log(O/H) \geq -3.5$, the main contributors to C and N should be massive stars. However, at intermediate metallicities, $-3.9 \leq \log(O/H) \leq -3.5$, the main contributors to C are low metallicity low-mass stars, but for N the main producers are massive stars and intermediate-mass stars of intermediate and low metallicity, respectively. Figure 12 shows a very large dispersion of the C/N ratio for halo stars, indicating that at very low metallicities the apparent coupling between N and C enrichments breaks. Here stochastic effects, bursting star formation or local variations on the enrichment process in the first stages of the galaxy formation could affect the abundance ratio of these elements across the halo.

The peculiar position of the star-forming knot of NGC 5253 labelled as A by López-Sánchez et al. (2007) in Figures 11 and 12 is due to the effect of localized pollution of material processed by the CNO cycle in massive Wolf-Rayet stars, as it has been confirmed by the results of different authors (Welch 1970; Walsh & Roy 1987, 1989; Kobulnicky et al. 1997; López-Sánchez et al. 2007; Monreal-Ibero et al. 2010). This knot shows strong enhancement of N – and perhaps He – while the abundances of

C and O remain quite constant across the object (e.g. López-Sánchez et al. 2007). This is the only star-forming dwarf galaxy where chemical pollution by massive Wolf-Rayet stars has been unambiguously detected. On the other hand, as we commented in §5.1, NGC 2363 is in a peculiar position in Figures 6 and 8 due to its high C/O ratio. In principle, following the arguments of Garnett et al. (1995) to explain the excess C/O ratios they found for I Zw 18, this fact may be interpreted as the effect of delayed ejection of fresh C from LIM stars due to a previous star-formation event in the host irregular galaxy. If this is the case, this object should also show some increase of the N/O ratio with respect to its metallicity due to the contribution of N produced by LIM stars. The position of NGC 2363 in Figure 11 seems to support this hypothesis because it follows the general C/O vs. N/O correlation and therefore the excess C/O seems to be associated with a somewhat higher N/O ratio. However, the position of NGC 2363 in Figure 12 seems to be slightly above the rest of the objects, and the presence of a small excess of C in the observed area of this object can not be ruled out.

6 CONCLUSIONS

We present deep echelle spectrophotometry of the brightest emission-line knots of the star-forming galaxies He 2–10, Mkn 1271, NGC 3125, NGC 5408, POX 4, SDSS J1253–0312, Tol 1457–262, Tol 1924–416, and the H II region Hubble V in the Local Group dwarf irregular galaxy NGC 6822. The spectra cover from 3550 to 10 400 Å and have been taken with the Ultraviolet-Visual Echelle Spectrograph attached to the UT2 of the Very Large Telescope at Cerro Paranal Observatory. We have derived consistent and precise values of the physical conditions for each object making use of several emission line-intensity ratios as well as abundances for several ionic species from the intensity of collisionally excited lines (CELs). We derive the ionic abundances of C²⁺ and/or O²⁺ from faint pure recombination lines (RLs) in several of the objects, permitting to derive their C/H and C/O ratios. For some objects, we have estimated the t^2 parameter from the analysis of the intensity ratios of He I lines as well as assuming that the ADF(O²⁺) is produced by temperature fluctuations, finding that both methods give in general consistent results. We find also that giant H II regions in dwarf star-forming galaxies present the highest ADF(O²⁺) and t^2 values among the inventory of determinations available for H II regions.

We have explored the chemical evolution in low-metallicity objects analysing the C/O vs. O/H relation and comparing with model results for the Milky Way. We find that H II regions in star-forming dwarf galaxies tend to show lower values of the C/O ratio and somewhat lower O/H than H II regions belonging to spiral galaxies, indicating their different chemical evolution histories. The comparison with C/O ratios in other objects indicate that the position of star-forming dwarf galaxies is similar to that of Galactic halo stars, suggesting the same origin for the bulk of C in those galaxies. We have also found that the dichotomy between the C/O ratios observed in stars of the Galactic thick and thin discs coincides with the systematic differences between the C/O ratios in H II regions belonging to spiral or dwarf star-

forming galaxies. This fact supports the merging scenario for the origin of the Galactic thick disc. Finally, we explore the C/O vs. N/O and C/N vs. O/H relations, finding that – at the usual metallicities determined for H II regions – there is an apparent coupling between C and N enrichment that may be due to the cumulative-temporal contribution of the C and N by stars of different masses. For very low-metallicity objects – as Galactic halo stars – such coupling breaks. This may be due to the bursting star-formation mode, stochastic effects, and/or local pollution in the first stages of the galaxy formation.

ACKNOWLEDGMENTS

We are very grateful to the referee, Grazyna Stasińska, for her very valuable and constructive comments and suggestions that have contributed to improve the final version of the paper. This work has been funded by the Spanish Ministerio de Economía y Competitividad (MINECO) under project AYA2011-22614. L. Carigi and M. Peimbert are grateful to the financial support provided by CONA-CyT of Mexico (grant 129753). L. Carigi also thanks financial support from project AYA2010-16717 funded by MINECO. A. Mesa-Delgado acknowledges support from a Basal-CATA (PFB-06/2007) grant and the FONDECYT project 3140383. This research has made use of the NASA/IPAC Extragalactic Database (NED) which is operated by the Jet Propulsion Laboratory, California Institute of Technology, under contract with the National Aeronautics and Space Administration. This research has made use of the SIMBAD database, operated at CDS, Strasbourg, France.

REFERENCES

- Aggarwal K. M., Keenan F. P., 1999, ApJS, 123, 311
- Akerman C. J., Carigi L., Nissen P. E., Pettini M., Asplund M., 2004, A&A, 414, 931
- Asplund M., Grevesse N., Sauval A. J., Scott P., 2009, ARA&A, 47, 481
- Bensby T., Feltzing S., 2006, MNRAS, 367, 1181
- Bonnarel F., Fernique P., Bienaymé O., Egret D., Genova F., Louys M., Oshenbein F., Wenger M., Bartlett J. G., 2000, A&AS, 143, 33
- Cardelli J. A., Clayton G. C., Mathis J. S., 1989, ApJ, 345, 245
- Carigi L., 2000, RMxAA, 36, 171
- Carigi L., Hernandez X., 2008, MNRAS, 390, 582
- Carigi L., Hernandez X., Gilmore G., 2002, MNRAS, 334, 117
- Carigi L., Peimbert M., Esteban C., García-Rojas J., 2005, ApJ, 623, 213
- Cescutti G., Matteucci F., McWilliam A., Chiappini C., 2009, A&A, 505, 605
- Chiappini C., Romano D., Matteucci F., 2003, MNRAS, 339, 63
- Cooke R., Pettini M., Murphy M. T., 2012, MNRAS, 425, 347
- Cooke R., Pettini M., Steidel C. C., Rudie G. C., Nissen P. E., 2011, MNRAS, 417, 1534

- Davey A. R., Storey P. J., Kisielius R., 2000, *A&AS*, 142, 85
- D’Odorico S., Cristiani S., Dekker H., Hill V., Kaufer A., Kim T., Primas F., 2000, in Bergeron J., ed., *Society of Photo-Optical Instrumentation Engineers (SPIE) Conference Series Vol. 4005 of Society of Photo-Optical Instrumentation Engineers (SPIE) Conference Series*, Performance of UVES, the echelle spectrograph for the ESO VLT and highlights of the first observations of stars and quasars. pp 121–130
- Esteban C., Bresolin F., Peimbert M., García-Rojas J., Peimbert A., Mesa-Delgado A., 2009, *ApJ*, 700, 654
- Esteban C., Carigi L., Copetti M. V. F., García-Rojas J., Mesa-Delgado A., Castañeda H. O., Péquignot D., 2013, *MNRAS*, 433, 382
- Esteban C., García-Rojas J., Mesa-Delgado A., Toribio San Cipriano L., 2014, *Astronomische Nachrichten*, 335, 73
- Esteban C., García-Rojas J., Peimbert M., Peimbert A., Ruiz M. T., Rodríguez M., Carigi L., 2005, *ApJ*, 618, L95
- Esteban C., Peimbert M., García-Rojas J., Ruiz M. T., Peimbert A., Rodríguez M., 2004, *MNRAS*, 355, 229
- Esteban C., Peimbert M., Torres-Peimbert S., Escalante V., 1998, *MNRAS*, 295, 401
- Esteban C., Peimbert M., Torres-Peimbert S., Rodríguez M., 2002, *ApJ*, 581, 241
- Fabbian D., Nissen P. E., Asplund M., Pettini M., Akerman C., 2009, *A&A*, 500, 1143
- Ferland G. J., Henney W. J., O’Dell C. R., Porter R. L., van Hoof P. A. M., Williams R. J. R., 2012, *ApJ*, 757, 79
- Froese Fischer C., Tachiev G., 2004, *Atomic Data and Nuclear Data Tables*, 87, 1
- Gail H.-P., Sedlmayr E., 1986, *A&A*, 166, 225
- Galavís M. E., Mendoza C., Zeppen C. J., 1995, *A&AS*, 111, 347
- García-Rojas J., Esteban C., 2007, *ApJ*, 670, 457
- Garnett D. R., 2004, in Esteban C., García López R., Herero A., Sánchez F., eds, *Cosmochemistry. The melting pot of the elements Element abundances in nearby galaxies*. pp 171–216
- Garnett D. R., Shields G. A., Peimbert M., Torres-Peimbert S., Skillman E. D., Dufour R. J., Terlevich E., Terlevich R. J., 1999, *ApJ*, 513, 168
- Garnett D. R., Skillman E. D., Dufour R. J., Peimbert M., Torres-Peimbert S., Terlevich R., Terlevich E., Shields G. A., 1995, *ApJ*, 443, 64
- Garnett D. R., Skillman E. D., Dufour R. J., Shields G. A., 1997, *ApJ*, 481, 174
- Guseva N. G., Izotov Y. I., Stasińska G., Fricke K. J., Henkel C., Papaderos P., 2011, *A&A*, 529, A149
- Hamuy M., Suntzeff N. B., Heathcote S. R., Walker A. R., Gigoux P., Phillips M. M., 1994, *PASP*, 106, 566
- Hamuy M., Walker A. R., Suntzeff N. B., Gigoux P., Heathcote S. R., Phillips M. M., 1992, *PASP*, 104, 533
- Henry R. B. C., Edmunds M. G., Köppen J., 2000, *ApJ*, 541, 660
- Hirschi R., 2007, *A&A*, 461, 571
- Hirschi R., Meynet G., Maeder A., 2005, *A&A*, 433, 1013
- Izotov Y. I., Stasińska G., Meynet G., Guseva N. G., Thuan T. X., 2006, *A&A*, 448, 955
- Izotov Y. I., Thuan T. X., 1999, *ApJ*, 511, 639
- Izotov Y. I., Thuan T. X., Lipovetsky V. A., 1994, *ApJ*, 435, 647
- Jenkins E. B., 2014, *ArXiv e-prints*
- Johansson S., Zethson T., Hartman H., Ekberg J. O., Ishibashi K., Davidson K., Gull T., 2000, *A&A*, 361, 977
- Karakas A., Lattanzio J. C., 2007, *Proc. Astron. Soc. Aust.*, 24, 103
- Karthick M. C., López-Sánchez Á. R., Sahu D. K., Sanwal B. B., Bisht S., 2014, *MNRAS*, 439, 157
- Kisielius R., Storey P. J., Ferland G. J., Keenan F. P., 2009, *MNRAS*, 397, 903
- Kobayashi C., Tominaga N., Nomoto K., 2011, *ApJ*, 730, L14
- Kobulnicky H. A., Skillman E. D., 1998, *ApJ*, 497, 601
- Kobulnicky H. A., Skillman E. D., Roy J.-R., Walsh J. R., Rosa M. R., 1997, *ApJ*, 477, 679
- Kroupa P., Tout C. A., Gilmore G., 1993, *MNRAS*, 262, 545
- Liu X.-W., Storey P. J., Barlow M. J., Danziger I. J., Cohen M., Bryce M., 2000, *MNRAS*, 312, 585
- López-Sánchez Á. R., Esteban C., 2008, *A&A*, 491, 131
- López-Sánchez Á. R., Esteban C., 2010, 517, A85
- López-Sánchez Á. R., Esteban C., García-Rojas J., 2006, *A&A*, 449, 997
- López-Sánchez Á. R., Esteban C., García-Rojas J., Peimbert M., Rodríguez M., 2007, *ApJ*, 656, 168
- Luridiana V., Morisset C., Shaw R. A., 2012, in *IAU Symposium Vol. 283 of IAU Symposium, PyNeb: a new software for the analysis of emission lines*. pp 422–423
- Maeder A., 1992, *A&A*, 264, 105
- Marigo P., Bressan A., Chiosi C., 1996, *A&A*, 313, 545
- Marigo P., Bressan A., Chiosi C., 1998, 331, 564
- Mathis J. S., 1996, in Holt S. S., Sonneborn G., eds, *Cosmic Abundances Vol. 99 of Astronomical Society of the Pacific Conference Series, The Composition of Interstellar Dust*. p. 327
- Mazzarella J. M., Boroson T. A., 1993, *ApJS*, 85, 27
- McConnachie A. W., 2012, *AJ*, 144, 4
- McLaughlin B. M., Bell K. L., 2000, *Journal of Physics B Atomic Molecular Physics*, 33, 597
- Mendoza C., Zeppen C. J., 1983, *MNRAS*, 202, 981
- Mesa-Delgado A., Esteban C., García-Rojas J., Luridiana V., Bautista M., Rodríguez M., López-Martín L., Peimbert M., 2009, *MNRAS*, 395, 855
- Meynet G., Maeder A., 2002, *A&A*, 390, 561
- Minchev I., Chiappini C., Martig M., 2013, 558, A9
- Monreal-Ibero A., Vílchez J. M., Walsh J. R., Muñoz-Tuñón C., 2010, *A&A*, 517, A27
- Nava A., Casebeer D., Henry R. B. C., Jevremovic D., 2006, *ApJ*, 645, 1076
- Palay E., Nahar S. N., Pradhan A. K., Eissner W., 2012, *MNRAS*, 423, L35
- Peimbert A., 2003, *ApJ*, 584, 735
- Peimbert A., Peimbert M., 2005, *RMxAC*, 23, 9
- Peimbert A., Peimbert M., 2010, *ApJ*, 724, 791
- Peimbert A., Peimbert M., Luridiana V., 2002, *ApJ*, 565, 668
- Peimbert A., Peimbert M., Ruiz M. T., 2005, *ApJ*, 634, 1056
- Peimbert M., 1967, *ApJ*, 150, 825
- Peimbert M., Costero R., 1969, *Boletín de los Observatorios Tonantzintla y Tacubaya*, 5, 3
- Peimbert M., Peimbert A., Ruiz M. T., 2000, *ApJ*, 541, 688

- Peimbert M., Sarmiento A., Fierro J., 1991, *PASP*, 103, 815
- Peimbert M., Torres-Peimbert S., Ruiz M. T., 1992, *RMxAA*, 24, 155
- Perez E., 1997, *MNRAS*, 290, 465
- Podobedova L. I., Kelleher D. E., Wiese W. L., 2009, *Journal of Physical and Chemical Reference Data*, 38, 171
- Porter R. L., Ferland G. J., Storey P. J., Detisch M. J., 2012, *MNRAS*, 425, L28
- Porter R. L., Ferland G. J., Storey P. J., Detisch M. J., 2013, *MNRAS*, 433, L89
- Portinari L., Chiosi C., Bressan A., 1998, *A&A*, 334, 505
- Quinet P., 1996, *A&AS*, 116, 573
- Quinn P. J., Hernquist L., Fullagar D. P., 1993, *ApJ*, 403, 74
- Rodríguez M., 1999, *A&A*, 348, 222
- Rodríguez M., Rubin R. H., 2005, *ApJ*, 626, 900
- Romano D., Karakas A. I., Tosi M., Matteucci F., 2010, *A&A*, 522, A32
- Ruiz M. T., Peimbert A., Peimbert M., Esteban C., 2003, *ApJ*, 595, 247
- Schönrich R., Binney J., 2009, *MNRAS*, 399, 1145
- Skillman E. D., Hidalgo S. L., Weisz D. R., Monelli M., Gallart C., Aparicio A., Bernard E. J., Boylan-Kolchin M., Cassisi S., Cole A. A., Dolphin A. E., Ferguson H. C., Mayer L., Navarro J. F., Stetson P. B., Tolstoy E., 2014, *ArXiv e-prints*
- Sofia U. J., Parvathi V. S., Babu B. R. S., Murthy J., 2011, *AJ*, 141, 22
- Spite M., Cayrel R., Plez B., Hill V., Spite F., Depagne E., François P., Bonifacio P., Barbuy B., Beers T., Andersen J., Molaro P., Nordström B., Primas F., 2005, *A&A*, 430, 655
- Stasińska G., 1978, *A&A*, 66, 257
- Stasińska G., 1990, *A&AS*, 83, 501
- Storey P. J., 1994, *A&A*, 282, 999
- Storey P. J., Hummer D. G., 1995, *MNRAS*, 272, 41
- Storey P. J., Sochi T., Badnell N. R., 2014, *MNRAS*, 441, 3028
- Tayal S. S., 2011, *ApJS*, 195, 12
- Tayal S. S., Zatsarinny O., 2010, *ApJS*, 188, 32
- Testor G., Lemaire J. L., Field D., 2003, *A&A*, 407, 905
- Verner E. M., Verner D. A., Baldwin J. A., Ferland G. J., Martin P. G., 2000, *ApJ*, 543, 831
- Villalobos A., Helmi A., 2009, in Andersen J., Nordström B., Bland-Hawthorn J., eds, *IAU Symposium Vol. 254 of IAU Symposium, Formation of thick disks*. p. 76
- Walsh J. R., Roy J.-R., 1987, *ApJ*, 319, L57
- Walsh J. R., Roy J.-R., 1989, *MNRAS*, 239, 297
- Weaver T. A., Woosley S. E., 1993, *Physics Reports*, 227, 65
- Welch G. A., 1970, *ApJ*, 161, 821
- Zhang H., 1996, *A&AS*, 119, 523